Monthly Notices of the ROYAL ASTRONOMICAL SOCIETY

MNRAS **546,** 1–18 (2026) https://doi.org/10.1093/mnras/stag097
Advance Access publication 2026 January 16

The Quasar Feedback Survey: revealing the importance of sensitive radio imaging for AGN identification deeper into the radio-quiet regime

Ann Njeri [1]★ Chris M. Harrison [1]★ Preeti Kharb [2] David M. Alexander,[3] Vincenzo Mainieri,[4] Chiara Circosta,[5] Victoria A. Fawcett [1] Darshan Kakkad [6] Dipanjan Mukherjee [7] Stephen Molyneux[8,9] and Silpa Sasikumar[10]

[1]*School of Mathematics, Statistics and Physics, Newcastle University, Newcastle upon Tyne NE1 7RU, UK*
[2]*National Centre for Radio Astrophysics (NCRA) – Tata Institute of Fundamental Research (TIFR), S. P. Pune University Campus, Post Bag 3, Ganeshkhind 411007, Pune, India*
[3]*Department of Physics, Centre for Extragalactic Astronomy, Durham University, South Road, Durham DH1 3LE, UK*
[4]*European Southern Observatory (ESO), Karl-Schwarzschild-Straße 2, D-85748 Garching bei München, Germany*
[5]*Institut de Radioastronomie Millimétrique (IRAM), 300 rue de la Piscine, F-38400 Saint-Martin-d'Hères, France*
[6]*Department of Physics, Astronomy and Mathematics, Centre for Astrophysics Research, University of Hertfordshire, Hatfield AL10 9AB, UK*
[7]*Inter-University Centre for Astronomy and Astrophysics, Post Bag 4, Pune University, Ganeshkhind 411007, Pune, India*
[8]*School of Physics and Astronomy, University of Southampton, Southampton SO17 1BJ, UK*
[9]*Institute of Theoretical Astrophysics, University of Oslo, P.O. Box 1029, Blindern, NO-0315 Oslo, Norway*
[10]*Departamento de Astronomìa, Universidad de Concepción, Avenida Esteban Iturra s/n Casilla 160-C,Concepción, Chile*

Accepted 2026 January 9. Received 2026 January 7; in original form 2025 October 6

ABSTRACT

We present new sub-arcsecond (∼0.3–1 arcsec; ∼1–3 kpc) Very Large Array imaging at 1.4 and 6 GHz of 29 optically selected [O III] luminous ($L_{[\rm OIII]} > 10^{42.1}$ erg s^{-1}) $z < 0.2$ quasars drawn from the expanded Quasar Feedback Survey (QFeedS; with $L_{1.4\,\rm GHz} = 10^{22.6}$–$10^{26.3}$ W Hz^{-1}). These 29 new objects occupy the low end of the radio-power distribution ($L_{1.4\,\rm GHz}$=$10^{22.63}$–$10^{23.45}$ W Hz^{-1}) in the QFeedS sample and are nominally 'radio quiet'. Despite this, we find widespread evidence of active galactic nucleus (AGN)-driven synchrotron activity. Nearly ∼ 31 per cent exhibit resolved radio structures on ∼0.1–20 kpc scales consistent with compact jets or wind-driven outflows, and ∼ 90 per cent display steep spectra ($\alpha \lesssim -1$) indicative of optically thin synchrotron emission. Combining morphology, spectral index, and brightness-temperature diagnostics, at least ∼ 38 per cent of the sample show clear AGN signatures that cannot be explained by star formation alone. These constitute the first results from the expanded QFeedS (now 71 quasars spanning ≈ 4 dex in radio power) and demonstrate that compact low-power jets and AGN shocks are common deep inside the radio-quiet regime. A thorough understanding of feedback processes from quasars, deep into the 'radio-quiet' regime, will be obtained by connecting these high-resolution radio observations with multiwavelength observations.

Key words: galaxies: active – galaxies: evolution – galaxies: jets – quasars: supermassive black holes – radio continuum: galaxies.

1 INTRODUCTION

The radio-quiet quasar population is the predominant sample in optically selected quasar samples, such as those from the Sloan Digital Sky Survey (SDSS; K. I. Kellermann et al. 2016). Despite being among the most luminous optical sources, radio-quiet quasars remain challenging to study in the radio due to their intrinsically weak emission, compact morphology, and ambiguous emission mechanisms (e.g. P. Padovani 2016; F. Panessa et al. 2019). These luminous active galactic nuclei (AGNs) remain largely unresolved at the spatial resolution of all sky radio surveys such as FIRST and NVSS[1] (e.g. K. I. Kellermann et al. 2016; C. Tadhunter 2016; T. V. McCaffrey et al. 2022), meaning that the radio emission is typically confined within the host galaxies, i.e. on scales smaller than a few kiloparsecs. However, extended radio structures with an AGN origin may exist on smaller scales if produced by jets or shocks due to AGN-driven outflows, which

★ E-mail: ann.njeri@newcastle.ac.uk (AN); christopher.harrison@newcastle.ac.uk (CH)

[1]These are the Faint Images of the Radio Sky at Twenty-cm survey (FIRST) and the NRAO VLA Sky Survey (NVSS) (R. H. Becker, R. L. White & D. J. Helfand 1995; J. J. Condon et al. 1998).

© The Author(s) 2026.
Published by Oxford University Press on behalf of Royal Astronomical Society. This is an Open Access article distributed under the terms of the Creative Commons Attribution License (https://creativecommons.org/licenses/by/4.0/), which permits unrestricted reuse, distribution, and reproduction in any medium, provided the original work is properly cited.

Downloaded from https://academic.oup.com/mnras/article/546/4/stag097/8427327 by University of Hertfordshire user on 18 February 2026

are young and/or frustrated by a dense interstellar medium (ISM; e.g. L. Klindt et al. 2019; F. Panessa et al. 2019; V. A. Fawcett et al. 2020).

Despite the lack of powerful radio jets, it is becoming increasingly clear that studying radio emission in detail is very important for understanding the feedback processes from radio-quiet quasars. For example, hydrodynamic simulations have demonstrated that low-power radio jets, characteristic of radio-quiet AGNs, can still exert significant influence on their host galaxies. This is particularly through their interactions with the ISM when the jets are closely inclined relative to the galactic disc and can drive strong shocks and accelerate the gas (e.g. M. Meenakshi et al. 2022; R. Tanner & K. A. Weaver 2022; D. Mukherjee 2025). Importantly, jets do not need to escape the host galaxy to affect star formation. Even when confined within the inner kiloparsecs, these jets can cause turbulence, heat cold gas, and regulate the local gas reservoir. These theoretical insights are particularly relevant for compact low-luminosity radio sources, whose sub-kpc sizes and steep spectral indices are consistent with jet–ISM interactions occurring at < 2 kpc scales, potentially in early or frustrated phases of feedback (e.g. J. Chilufya et al. 2024; A. Njeri et al. 2025). Furthermore, quasar-driven winds could cause similar signatures in the extended radio emission, since they propagate as multiphase outflows through the ISM, shocking the material to produce synchrotron emission (e.g. J. Nims, E. Quataert & C.-A. Faucher-Giguère 2015; N. L. Zakamska et al. 2016; M. Meenakshi et al. 2024). While these processes can mimic starburst-driven outflows in the optical line kinematics, careful radio morphological and spectral analysis, such as identifying steep-spectrum, compact structures, and high brightness temperatures, can distinguish AGNs from star formation origins (e.g. M. E. Jarvis et al. 2021; L. K. Morabito et al. 2022; A. Njeri et al. 2025).

A key open question in galaxy evolution is the contribution to feedback from low-power and compact radio jets and quasar-driven winds in radio-quiet quasars. While classical radio-loud quasars with powerful jets are well established as efficient regulators of gas cooling for massive galaxies (e.g. A. C. Fabian 2012; T. M. Heckman & P. N. Best 2014; C. M. Harrison 2017), the impact of faint or compact structures, such as frustrated jets and disc winds, remains less clear (e.g. A. Laor & E. Behar 2008; F. Panessa et al. 2019; R. D. Baldi 2023). Recent studies suggest that even in radio-quiet quasars, small-scale jets and outflows can efficiently couple to the ISM on small scales, driving turbulence and modest outflows (e.g. M. E. Jarvis et al. 2019; G. Venturi et al. 2021; A. Audibert et al. 2023; G. Cresci et al. 2023; P. Kharb & S. Silpa 2023; R. Morganti et al. 2023; L. Ulivi et al. 2024; D. Mukherjee 2025). Determining whether such processes represent a significant feedback mode, and how efficiently they regulate star formation, is crucial for building a complete picture of AGN-galaxy co-evolution.

A related challenge is how can we robustly separate star formation from AGN-driven radio emission, and establishing what this reveals about the spectrum of feedback modes in quasars. This complicates efforts to assess the star formation rates at quasar luminosities and raises questions about how feedback scales across the radio luminosity function. The emerging view is that quasars span a continuum of radio modes, from weak AGN-contaminated synchrotron at low luminosities to powerful jet-dominated systems at high luminosities (e.g. N. L. Zakamska & J. E. Greene 2014; J. Sabater et al. 2019; M. E. Jarvis et al. 2021; A. Girdhar et al. 2022; M. M. Slob et al. 2022). This spectrum challenges the traditional binary classification of 'radio-loud' versus 'radio-quiet' AGNs and motivates a more continuum between accretion states, production of radio emission, and efficiency of feedback (e.g. P. Padovani 2017; M. J. Hardcastle & J. H. Croston 2020; B. Mingo et al. 2022).

Towards addressing the outstanding issues outlined above, we have been undertaking a systematic survey of low redshift Type 1 and Type 2 ($z < 0.2$) quasars, called the 'Quasar Feedback Survey' (QFeedS; M. E. Jarvis et al. 2021).[2] The primary objectives of this survey include (1) understanding the origin of radio emission in sources with moderate-to-low radio luminosities; (2) characterizing the properties of multiphase outflows in the quasar host galaxies; and, (3) assessing the potential long-term impact of the central quasar on the host galaxies.

In this work we introduce our first results on the radio properties from a new sample, exploring deeper into the radio-quiet regime ($L_{1.4\,\mathrm{GHz}} < 10^{23.4}\,\mathrm{W\,Hz^{-1}}$) than our earlier work ($L_{1.4\,\mathrm{GHz}} > 10^{23.4}\,\mathrm{W\,Hz^{-1}}$). In Section 2 we introduce the QFeedS and describe the new sample for this work (QFeedS-2). In Section 3 we describe the observations and imaging methods for the new radio data, before discussing the results in Section 4. In Section 5 we discuss our new results in the context of the wider QFeedS sample and other AGN populations and present our main conclusions in Section 6. We adopt $H_0 = 70\,\mathrm{km\,s^{-1}\,Mpc^{-1}}$, $\Omega_M = 0.3$, and $\Omega_\Lambda = 0.7$ throughout. In this cosmology, 300 mas (i.e. our typical resolution at ~ 6.0 GHz) corresponds to ~ 0.8 kpc for the median redshift of the sample (z=0.15). We define the radio spectral index, ν, using $S_\nu \propto \nu^\alpha$.

2 THE QUASAR FEEDBACK SURVEY

In this section we present an overview of QFeedS and the motivation for the new sample (Section 2.1), before describing in more detail the sample used in this work (Section 2.2 and Section 2.3).

2.1 Survey description

The initial sample of 42 quasars (QFeedS-1) was fully introduced in M. E. Jarvis et al. (2021), although this followed multiple pilot studies (e.g. C. M. Harrison et al. 2014, 2015; G. B. Lansbury et al. 2018; M. E. Jarvis et al. 2019). The goal of QFeedS is to build up a multiwavelength picture of feedback from quasars, e.g. covering radio imaging and multiphase outflow measurements. Quasars for QFeedS are selected to be low-redshift ($z < 0.2$) luminous [O III] emitters ($L_{[\mathrm{OIII}]} \gtrsim 10^{42}\,\mathrm{erg\,s^{-1}}$) from the AGN sample presented in J. R. Mullaney et al. (2013), who used spectroscopy from the SDSS, Data Release 7 (K. N. Abazajian et al. 2009). This redshift and luminosity selection criteria enables high spatial resolution observations (reaching sub-kiloparsec resolution) of sources that have quasar-like AGN luminosities ($L_{\mathrm{AGN}} \gtrsim 10^{45}\,\mathrm{erg\,s^{-1}}$). These luminosities are equivalent to the knee of the luminosity function around cosmic noon (see M. E. Jarvis et al. 2020, 2021). Therefore, this survey is complementary to surveys of more nearby radiatively luminous AGNs, which cover typically lower bolometric powers or smaller samples (e.g. R. A. Riffel et al. 2017; M. Rose et al. 2018; R. Davies et al. 2020; A. Fluetsch et al. 2021; S. García-Burillo et al. 2021; G. Venturi et al. 2021), or those

[2] A survey website, including results, information on targets and open access to our data products/images can be found here: (https://blogs.ncl.ac.uk/quasarfeedbacksurvey/).

Downloaded from https://academic.oup.com/mnras/article/546/4/stag097/8427327 by University of Hertfordshire user on 18 February 2026

that focus on radio galaxies (e.g. R. Morganti, C. N. Tadhunter & T. A. Oosterloo 2005; F. Santoro et al. 2020; G. Speranza et al. 2021). It also complements those that focus on higher redshifts, which reach higher luminosities but with more limited sensitivity and spatial resolution (e.g. N. P. H. Nesvadba et al. 2017; C. Circosta et al. 2018; G. S. Ilha et al. 2025; N. Roy, T. Heckman & A. Henry 2025).

Similar surveys at the redshift range of QFeedS also cover multiwavelength approaches to understanding AGN feedback in quasars (e.g. M. Karouzos, J.-H. Woo & H.-J. Bae 2016; C. Ramos Almeida et al. 2022; P. S. Bessiere et al. 2024). However, unlike most other surveys of radiatively luminous AGNs, a key part of QFeedS has been to start by obtaining complete coverage with high spatial resolution radio imaging. Specifically, we have focused on the *C* band (4–8 GHz) and *L* band (1–2 GHz) from both the Very Large Array (VLA; M. E. Jarvis et al. 2019, 2021) and *e*-MERLIN (A. Njeri et al. 2025). Combining these new observations, with data from NVSS and FIRST, this has enabled us to create multifrequency radio images of these quasars, which are sensitive to structures on scales of ~ 0.05 arcsec (i.e. $\sim$0.1 kpc) to several arcseconds (i.e. 10s kpc).

Our initial sample of 42 targets (QFeedS-1) was selected to have radio luminosities of $L_{1.4\,\mathrm{GHz}} > 10^{23.45}\,\mathrm{W\,Hz^{-1}}$. The sample is presented in an [O III] luminosity versus 1.4 GHz luminosity plane in Fig. 1. It can be seen that, despite a minimum radio luminosity cut, the majority ($\sim$90 per cent) are still consistent with traditional definitions of 'radio quiet' (see discussion in M. E. Jarvis et al. 2021). However, based on on a variety of radio-AGN selection criteria (i.e. radio morphology, radio–infrared excess parameter, core spectral indices, and brightness temperatures), $86^{+4.6}_{-6.2}$ per cent reveal a radio AGN (M. E. Jarvis et al. 2021; A. Njeri et al. 2025). Furthermore, radio sizes are 0.03–65 kpc, covering the same size range of archetypal compact radio galaxy populations (e.g. T. An & W. A. Baan 2012), but with one to three orders of magnitude lower radio luminosities. Two-thirds of the sample show distinct radio structures, often indicative of jets and lobes (e.g. see fig. 4 in M. E. Jarvis et al. 2021 and fig. 7 in A. Njeri et al. 2025). These results highlight the important contribution of AGNs to the radio emission of quasars even with moderate radio luminosities (i.e. for 'radio-quiet' quasars; also see e.g. S. V. White et al. 2015, 2017; N. L. Zakamska et al. 2016).

Follow-up multiwavelength observations of QFeedS-1 targets give insight into feedback mechanisms in these sources. For example, spatially unresolved sub-mm emission-line observations suggest little immediate impact on the global molecular gas reservoirs in the host galaxies by the quasars in these systems (M. E. Jarvis et al. 2020; S. J. Molyneux et al. 2024). However, spatially resolved observations show a strong localized connection between the radio structures and high levels of turbulence and outflows, revealed through optical integral field spectroscopy (C. M. Harrison et al. 2015; M. E. Jarvis et al. 2019; A. Girdhar et al. 2022); sub-mm interferometry (A. Girdhar et al. 2022, 2024); and X-rays (G. B. Lansbury et al. 2018). Follow-up polarization-sensitive radio imaging has revealed a high fractional polarization (10–30 per cent) in the sources with the largest radio lobes, which provides further evidence of an interplay of jets or winds and emission-line gas as an important contribution to the nature of radio outflows in radio-quiet AGNs (S. Silpa et al. 2022). These observations are broadly consistent with simulations that show low power jets, confined within galaxy discs can drive outflows and have a feedback effect on their hosts, with potential additional contributions from outflow-driven shocks (e.g. D. Mukherjee et al. 2018; M. Meenakshi et al. 2022, 2024; R. Tanner & K. A. Weaver 2022).

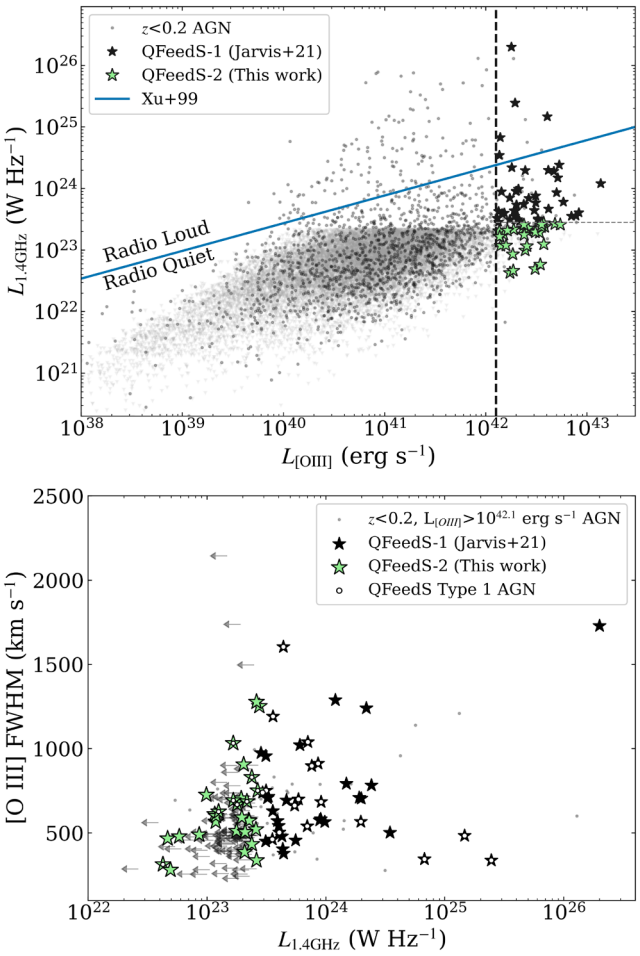

Figure 1. Top: 1.4 GHz radio luminosity versus [O III] luminosity for the parent sample of $z < 0.2$ AGNs (grey circles, with radio upper limits represented as lighter grey triangles; J. R. Mullaney et al. 2013). The dashed vertical line shows our quasar luminosity threshold for selection ($L_{[\mathrm{OIII}]} > 10^{42.11}\,\mathrm{erg\,s^{-1}}$). Bottom: [O III] FWHM versus 1.4 GHz radio luminosity for the parent sample above the [O III] luminosity cut (grey dots, with upper limits represented as arrows). In both panels the initial 42 QFeedS targets are represented with black stars (QFeedS-1), for which we imposed a minimum radio luminosity threshold ($L_{1.4\mathrm{GHz}} > 10^{23.45}\,\mathrm{W\,Hz^{-1}}$; dashed horizontal line in top panel). The 29 new targets, which are selected to be below this radio luminosity (QFeedS-2), are represented with green stars. Type 1 quasars are highlighted with white circles in the bottom panel.

The results from QFeedS-1 reveal important information on the prevalence of radio AGNs and how feedback works in a sample of mostly traditionally radio-quiet quasars. However, we are unable to address how representative these results are to the wider quasar population, reaching lower radio luminosities. Therefore, in this work, we present a new sample, QFeedS-2, reaching an order of magnitude lower in radio luminosity. With this, we can investigate the radio properties and feedback processes over several orders of magnitude in radio power and place them even more completely into the context of other AGN populations (following e.g. M. J. Hardcastle & J. H. Croston 2020; M. E. Jarvis et al. 2021; R. D. Baldi 2023).

Downloaded from https://academic.oup.com/mnras/article/546/4/stag097/8427327 by University of Hertfordshire user on 18 February 2026

Table 1. Key properties for the 29 QFeedS-2 targets. (1) Source ID; (2 and 3) optical positions (J2000); (4) redshifts from SDSS DR7; (5) AGN type from the optical spectra; (6 and 7) [O III] luminosity and FWHM from J. R. Mullaney et al. (2013); (8 and 9) integrated 1.4 GHz flux density and peak flux density from FIRST; (10) 1.4 GHz radio luminosity (based on NVSS; J. R. Mullaney et al. 2013).

Source ID	RA	Dec.	z	Type	$\log(L_{[OIII]})$ (/erg s^{-1})	FWHM$_{[OIII]}$ (km s^{-1})	S_{FIRST} (mJy)	P_{FIRST} (mJy beam^{-1})	$\log(L_{1.4\,GHz})$ (/W Hz^{-1})
(1)	(2)	(3)	(4)	(5)	(6)	(7)	(8)	(9)	(10)
J0213+0042	02:13:59.78	+00:42:26.8	0.182	1	42.68	752	2.90±0.12	3.16±0.07	23.43
J0232−0811	02:32:24.25	−08:11:40.2	0.100	2	42.15	567	3.48±0.12	3.77±0.08	23.07
J0827+2233	08:27:11.22	+22:33:24.2	0.173	2	42.37	576	2.03±0.13	2.03±0.07	23.35
J0841+0101	08:41:35.09	+01:01:56.3	0.111	2	42.41	388	3.51±0.19	2.50±0.09	23.32
J0924+1504	09:24:35.36	+15:04:10.0	0.125	2	42.39	727	3.43±0.09	3.22±0.05	22.99
J0947+1005	09:47:33.22	+10:05:08.8	0.139	1	42.18	669	1.41±0.10	1.21±0.05	23.25
J1034+6001	10:34:08.60	+60:01:52.2	0.051	2	42.41	612	18.98±0.19	16.78±0.10	23.06
J1110+5848	11:10:15.25	+58:48:46.0	0.143	2	42.42	574	4.11±0.21	3.90±0.12	23.35
J1141+2156	11:41:16.16	+21:56:21.8	0.063	1	42.24	314	2.68±0.45	1.80±0.20	22.63
J1152+1016	11:52:45.66	+10:16:23.8	0.070	2	42.27	468	3.57±0.08	3.39±0.05	22.67
J1203+1624	12:03:00.20	+16:24:43.8	0.166	2	42.74	339	2.91±0.13	2.90±0.07	23.42
J1300+5454	13:00:38.10	+54:54:36.9	0.088	2	42.49	282	2.16±0.13	1.96±0.07	22.69
J1316+4452	13:16:39.75	+44:52:35.1	0.091	2	42.20	602	4.30±0.13	3.96±0.07	23.07
J1325+1137	13:25:52.16	+11:37:09.8	0.161	1	42.58	831	2.84±0.10	2.93±0.06	23.38
J1338+1503	13:38:06.53	+15:03:56.1	0.185	2	42.53	705	2.22±0.09	1.91±0.05	23.29
J1355+5612	13:55:16.55	+56:12:44.7	0.122	1	42.28	688	6.04±0.15	5.88±0.08	23.34
J1410+2233	14:10:41.50	+22:33:37.1	0.173	1	42.14	1033	3.11±0.19	2.23±0.09	23.22
J1419+1144	14:19:43.79	+11:44:26.2	0.124	2	42.27	491	2.94±0.13	2.54±0.07	22.93
J1426+1040	14:26:14.62	+10:40:13.0	0.137	2	42.38	513	1.96±0.12	2.03±0.07	23.25
J1426+1949	14:26:26.93	+19:49:54.4	0.175	2	42.13	906	1.15±0.06	1.44±0.04	23.31
J1434+5016	14:34:11.18	+50:16:40.8	0.199	2	42.38	522	2.75±0.13	2.84±0.08	23.41
J1440+5303	14:40:38.10	+53:30:15.9	0.038	2	42.49	593	59.21±0.30	57.20±0.17	23.29
J1450+0713	14:50:34.12	+07:31:32.3	0.154	2	42.22	507	1.71±0.27	1.56±0.15	23.32
J1507+0029	15:07:19.94	+00:29:05.0	0.182	2	42.57	1254	4.36±0.11	4.40±0.06	23.44
J1529+5616	15:29:07.46	+56:16:06.7	0.100	1	42.57	627	4.26±0.13	4.31±0.08	23.10
J1543+1148	15:43:03.83	+11:48:38.5	0.098	2	42.54	479	2.09±0.11	2.60±0.07	22.77
J1653+2349	16:53:15.05	+23:49:43.0	0.103	2	42.55	435	7.14±0.12	6.72±0.07	23.38
J1713+5729	17:13:50.32	+57:29:54.9	0.113	2	42.55	1278	7.38±0.09	7.29±0.05	23.42
J2304−0841	23:04:43.48	−08:41:08.6	0.047	1	42.14	693	21.51±0.75	17.85±0.38	23.22

2.2 Sample selection for this work

Our goal is to expand the survey selection for QFeedS presented in M. E. Jarvis et al. (2021), to quasars with lower radio luminosities..[3] Therefore, we follow M. E. Jarvis et al. (2021), and choose $z < 0.2$ AGNs from J. R. Mullaney et al. (2013) with a luminosity $L_{[OIII]} > 10^{42.11}$ erg s^{-1}. This leaves a potential sample of 226 targets. We then exclude any sources with a declination between 24 and 44 deg, to avoid observing targets that transit with very high elevations above the VLA.[4]

For the initial sample of 42 targets we applied a radio luminosity selection of $L_{1.4GHz} > 10^{23.45}$ W Hz^{-1}. These 42 sources are labelled as 'QFeedS-1' in a $L_{1.4GHz}$ versus $L_{[OIII]}$ diagram in the top panel of Fig. 1. To create the new sample, we observed the remaining 29 sources that have a 1.4 GHz detection (in NVSS or FIRST) but with luminosities below the $L_{1.4GHz} = 10^{23.45}$ W Hz^{-1} luminosity threshold. The lower luminosity sample, which is new for this work, is labelled as 'QFeedS-2' in Fig. 1. We list key properties of the new QFeedS-2 sample in Table 1.

2.3 New sample overview

This new work brings our total sample in the QFeedS to 71 $z < 0.2$ targets, all of which have been selected to have high [O III] luminosities, corresponding to bolometric luminosities of $L_{bol} \gtrsim 10^{45}$ erg s^{-1} (see M. E. Jarvis et al. 2020). Of the 29 targets in QFeedS-2, eight are classified as Type 1 and 21 are classified as Type 2 based on their optical spectroscopy (J. R. Mullaney et al. 2013). Across the combined sample (QFeedS-1 and QFeedS-2), 25 (35 per cent) are classified as Type 1 and 46 (65 per cent) are classified as Type 2. This is representative of the parent sample of AGNs from J. R. Mullaney et al. (2013), which meet the redshift and [O III] luminosity cuts, for which 88/226 (i.e. 39 per cent) are confirmed as Type 1 AGNs.

For our [O III] luminosity and redshift selection criteria (see Fig. 1); $52^{+3.3}_{-3.3}$ per cent of the parent sample have radio detections in FIRST/NVSS from J. R. Mullaney et al. (2013). Our combined sample still does not represent the targets from the parent sample that only have upper limits on their 1.4 GHz radio luminosities based on FIRST and NVSS. The non-radio-detected sources have a mean upper limit of 1.9×10^{23} W Hz^{-1}, with a range of (0.27–2.7)$\times10^{23}$ W Hz^{-1}. None the less, the combined QFeedS sample covers nearly four orders of magnitude in radio luminosity from

[3]We calculate the radio luminosities using the 1.4 GHz flux densities for each source provided by J. R. Mullaney et al. (2013) (i.e. those taken from NVSS with preference, or FIRST otherwise) and assuming a spectral index of $\alpha = -0.7$. For the non-radio-detected sources, we use a flux density of 2.5 mJy to derive luminosity upper limits, corresponding to the 50 per cent completeness of the NVSS survey (J. J. Condon et al. 1998)

[4]We note that for the initial sample we also only considered targets in the RA range of 10–360 deg, for more efficient observation scheduling.

Downloaded from https://academic.oup.com/mnras/article/546/4/stag097/8427327 by University of Hertfordshire user on 18 February 2026

$L_{1.4\mathrm{GHz}}$=$10^{22.6}$ to $10^{26.3}$ W Hz^{-1}. Indeed, the sample expands deep into the 'radio-quiet' regime following the definition of C. Xu, M. Livio & S. Baum (1999) (see blue line in Fig. 1).

All targets in the QFeedS-2 sample are classified as 'radio quiet', with at least one order of magnitude lower radio luminosities than the 'radio-loud' cut-off. For the Type 1 targets, we additionally investigated the radio-loudness parameter, R, which compares radio to optical continuum luminosity as a means to define sources as 'radio loud'. Following K. I. Kellermann et al. (1989) and Ž. Ivezić et al. (2002), $R = 0.4(m_i - t)$, where m_i is the $i-$band magnitude from SDSS DR16 (R. Ahumada et al. 2020) and t is the 'AB radio magnitude' given by $t = -2.5 \log\left(\frac{S_{1.4\,\mathrm{GHz}}}{3631\mathrm{Jy}}\right)$, none of the Type 1 targets in QFeedS-2 pass the radio-loudness criteria of $R \gtrsim 1.0$. In contrast, in the initial sample (QFeedS-1), nine targets were classified as 'radio loud' following both criteria. Furthermore, many targets in the QFeedS-1 sample could be classified as 'radio intermediate', due to their proximity to the radio-loud/quiet boundary (M. E. Jarvis et al. 2021).

In the bottom panel of Fig. 1 we show [O III] full width at half-maximum (FWHM) as a function of radio luminosity for the parent sample in the redshift and [O III] luminosity range of our selection, and highlight the QFeedS targets with larger symbols. In this figure the plotted FWHM is the flux-weighted average of the two components that are fitted to the [O III] emission lines in the SDSS spectra, following J. R. Mullaney et al. (2013). It can be seen that the combined QFeedS sample covers the full range of FWHM parameter space of the parent sample. Furthermore, the figure re-highlights the previously identified increased fraction of extreme kinematics ($\gtrsim$800 km s^{-1}) for radio luminosities greater than $\sim 2 \times 10^{23}$ W Hz^{-1} (J. R. Mullaney et al. 2013; also see N. L. Zakamska & J. E. Greene 2014, J.-H. Woo et al. 2016, M. E. Jarvis et al. 2021).

The new QFeedS-2 sample provides the opportunity to study the radio properties of quasars over multiple orders of magnitude in radio luminosity, and explore deep into the 'radio-quiet' regime. Building on the work with QFeedS-1, future multiwavelength follow-up observations will enable an assessment of the connection between radio emission and multiphase outflows across the quasar population. In this work, we present new L-band and C-band VLA observations of the 29 QFeedS-2 targets, following similar approaches to the equivalent data presented for the initial 42 QFeedS-1 targets in M. E. Jarvis et al. (2019, 2021) and with C-band e-MERLIN data in A. Njeri et al. (2025). We then combine and compare the radio properties of the full sample (QFeedS-1 and QFeedS-2), and explore the possible origin of the radio emission across the full radio luminosity range.

3 OBSERVATIONS AND DATA REDUCTION

Observations of the 29 quasars (QFeedS-2) were conducted with VLA in the L band (1.2–1.7 GHz) and C band (5.25–7.20 GHz), under the proposal ID 23A-214 [PI. Njeri]. These observations were carried out between 2023 July and September using the A array, providing a representative resolution of 1.0 and 0.3 arcsec, in the L band and C band, respectively. While all targets were covered by the C-band observations, three targets were not observed in the L band (J0213+0042, J0232−0811, and J2304−0841), due to incompleted observations. We observed for 10.5 h in L band (5–30 min per source) and 9.5 h in C band (5–30 min per source). Each target was observed in at least two scans spread across 1–2 h observing blocks. At the start of each observing block, a standard calibrator (3C286, 3C48, or 3C147) was observed for ∼10 min. A phase calibrator was observed for ∼3 min per scan (including the slewing time) followed by the target.

We used the VLA Calibration Pipeline 2024.1.0.8 for CASA version 6.6.1 to reduce our data. The calibrated measurement set was then inspected using CASA task PLOTMS and any remaining bad data was visually identified and flagged using 'tfcrop' mode in CASA task FLAGDATA. Each target was split into their own measurement set and imaged using CASA task TCLEAN. Maps of 2500 × 2500 cells were constructed, with a cell size of 0.2 arcsec per pixel for L band, and 0.06 arcsec per pixel for C band. To produce a consistent set of images to QFeedS-1 we followed M. E. Jarvis et al. (2021) and used a Briggs weighting of $r = 0.5$ for all radio maps. This provides a suitable compromise between sensitivity to larger scale structures and higher spatial resolution. This uniform approach is most suitable for this systematic study, but we note that a source-by-source imaging optimization can sometimes reveal additional structures or detail (e.g. comparing different approaches for the same targets in M. E. Jarvis et al. 2021 and M. E. Jarvis et al. 2019). We generated radio maps with typical median root-mean square (rms) sensitivities of $\sim$ 24 μJy beam^{-1} in L band and $\sim$ 10 μJy beam^{-1} in C band. In comparison, the QFeedS-1 radio maps were produced at typical median rms sensitivities of $\sim$ 47 μJy in L band and $\sim$ 12 μJy beam^{-1} in C band.

Examples of these radio maps are presented in Fig. 2 and Fig. 3, which showcase a range of the morphological structures observed (see Section 4.1). The background optical images are from the archival three-colour (RGB) image from the Dark Energy Spectroscopic Instrument (DESI) Legacy Imaging Survey using the z, r, g bands (A. Dey et al. 2019). Overlaid are contour maps from the VLA FIRST survey in white, and our VLA L-band and C-band maps in green and blue, respectively. We release all the equivalent figures for the whole sample and all the radio maps, which include all of the relevant metadata (e.g. the exact beam sizes for each map; see Data Availability section).

To extract the radio properties such as the total flux density, peak flux density, and the linear size of radio components, the targets were fitted using the CASA task IMFIT. These measured values are presented in Table 2. Where distinct multiple components were identified in an individual source, these properties have been extracted separately (i.e. those classified as doubles or triples; see Section 4.1).

We also produced spectral index (α) maps using the C-band data. We applied the two Taylor terms to model the frequency dependence of the sky emission and generated the in-band (5.25–7.20 GHz) spectral index maps and corresponding error maps. To extract the spectral indices of the core regions, and the associated errors, we took the median value of the α image within a region that covered the core only and obtained the equivalent error from the respective error maps (see Section 4.3). These α values and the corresponding errors are presented in Table 2.

4 RESULTS

Building on the work presented in M. E. Jarvis et al. (2021) and A. Njeri et al. (2025), one of the primary goals of QFeedS is to establish the fraction of moderate-to-low radio luminosity quasars (average $\sim L_{1.4\,\mathrm{GHz}} \approx 10^{23.5}$ W Hz^{-1}) that show radio emission associated with AGN processes. In this work, we present the results from the new QFeedS-2 sample, which comprises of 29 targets in a luminosity range of $L_{1.4\,\mathrm{GHz}} \sim 10^{22.63}$–$10^{23.45}$ W Hz^{-1}, pushing

Downloaded from https://academic.oup.com/mnras/article/546/4/stag097/8427327 by University of Hertfordshire user on 18 February 2026

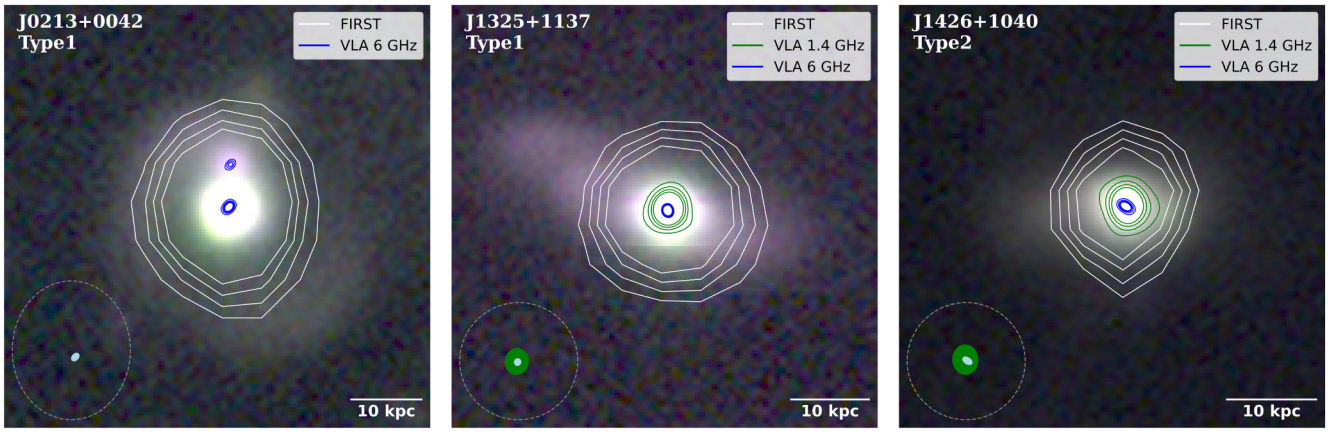

Figure 2. Examples of our radio data for sources classified as compact based on radio morphology in the QFeedS-2 sample (see Section 4.1). The RGB images come from the DESI Legacy Imaging Survey in the *z*, *r*, *g* bands. The contours overlaid represent FIRST maps in white with levels $1\sigma \times [2, 3, 4, 5]$; our new VLA 1.4 GHz maps in green with levels $1\sigma \times [2, 4, 6, 8]$ (except for J0213+0042, which was not observed); and our new VLA 6 GHz maps in blue with levels $1\sigma \times [2, 4, 6, 8]$. The ellipses represent the synthesized beam for the corresponding radio map contours; ∼5 arcsec for FIRST (in dashed grey ellipses), ∼1 arcsec for VLA 1.4 GHz (in green), and ∼0.3 arcsec for VLA 6 GHz (in light blue). The scale bar highlights the physical size scales. Equivalent figures for all sources are provided (see the Data Availability section). For J0213+0042, we note the target was classified as a 'compact' source because the second radio component, which coincides with a second optical companion, was ignored.

further into the radio-quiet regime than in the initial QFeedS-1 sample (see Fig. 1).

We present three sets of radio maps, those from the archival FIRST data, and our new *L*-band and *C*-band VLA maps (Section 3). Accounting for the redshift range of the sample, these maps cover a spatial resolution of ∼ 5–20 kpc in the 1.4 GHz FIRST images, ∼ 1–20 kpc in our new *L*-band (1.4 GHz) maps and ∼ 0.3–1 kpc in our new *C*-band (6 GHz) maps. Example maps are shown in Fig. 2 and Fig. 3. The measured radio properties are presented in Table 2.

In Section 4.1, we present the radio morphology classification based on visual inspection and we present the results of largest linear size (LLS) measurements in Section 4.2. In Section 4.3 and Section 4.4, we present the spectral index and brightness temperature measurements, respectively. In Section 4.5, we summarize how the radio measurements (morphology, brightness temperature, and spectral index) were used for the final identification of 'radio AGNs'.

4.1 Detected radio structures and their morphology

Detecting and characterizing radio structures across the quasar sample provides crucial insights into the physical mechanisms driving radio emission and its potential role in feedback. Following the nomenclature used in M. E. Jarvis et al. (2021), we classify our targets as follows:

(i) Compact (C): when only a single compact structure is identified.

(ii) Double (D): the target has two clearly distinct radio peaks.

(iii) Triple (T): the target has three clearly distinct radio peaks.

(iv) Jet-like (J): when the targets show a single central radio component and are visibly spatially extended in one or two directions. In this category, we also include two sources (J0841+0101 and J1300+5454) with some more irregular structures for which two or three individual components are not well defined, but are generally collimated and jet-like.

Since the targets remained largely compact and unresolved in FIRST and only a few sources (J0841+0101, J1034+6001, J1300+5454, and J1316+4452) showed visibly extended emission in *L*-band maps, we used the *C*-band radio maps for the radio morphology classification. There are two sources (J0213+0042 and J1410+2233) that show radio emission associated with secondary optical counterparts. Consequently, the radio structures are likely associated with companion galaxies and we ignored these radio structures in the classifications.

We find that 20/29 sources were classified as compact, with three examples shown in Fig. 2. For the nine sources that show extended radio structures from the visual classification, 6/9 are classified as jet-like, 1/9 is classified as a double, and 2/9 are classified as triples. All nine of these sources are presented in Fig. 3. For simplicity, and for the remainder of this work, all extended emission and well-collimated multiple components (double or triple radio peaks) are considered as jet-like (following our radio morphology classification presented in A. Njeri et al.; 2025). However, we note that this purely defines the radio morphology and does not necessarily indicate the presence of a traditional AGN-driven jet (further discussion in Section 5.2).

In summary, a total of 9/29 targets (∼ 31 per cent) show extended radio structures in the QFeedS-2 sample. This is in contrast to QFeedS-1, for which $67^{+6.8}_{-7.6}$ per cent showed extended structures using equivalent datasets, and we discuss the variations across the whole of QFeedS further in Section 5.1 (also see similar examples from other samples in E. Middelberg et al. 2007; R. D. Baldi et al. 2018; C. P. O'Dea & D. J. Saikia 2021).

4.1.1 Comparison with FIRST and implications for diffuse emission

To assess how much large-scale low-surface-brightness radio emission might be missed by our higher resolution *L*-band data, we compare the integrated flux density measured in our *L*-band maps with the FIRST integrated flux densities (both at 1.4 GHz). We report the per-source flux ratio:

$$R = \frac{S_{1.4\,\mathrm{GHz}}}{S_{\mathrm{FIRST}}} \quad (1)$$

Downloaded from https://academic.oup.com/mnras/article/546/4/stag097/8427327 by University of Hertfordshire user on 18 February 2026

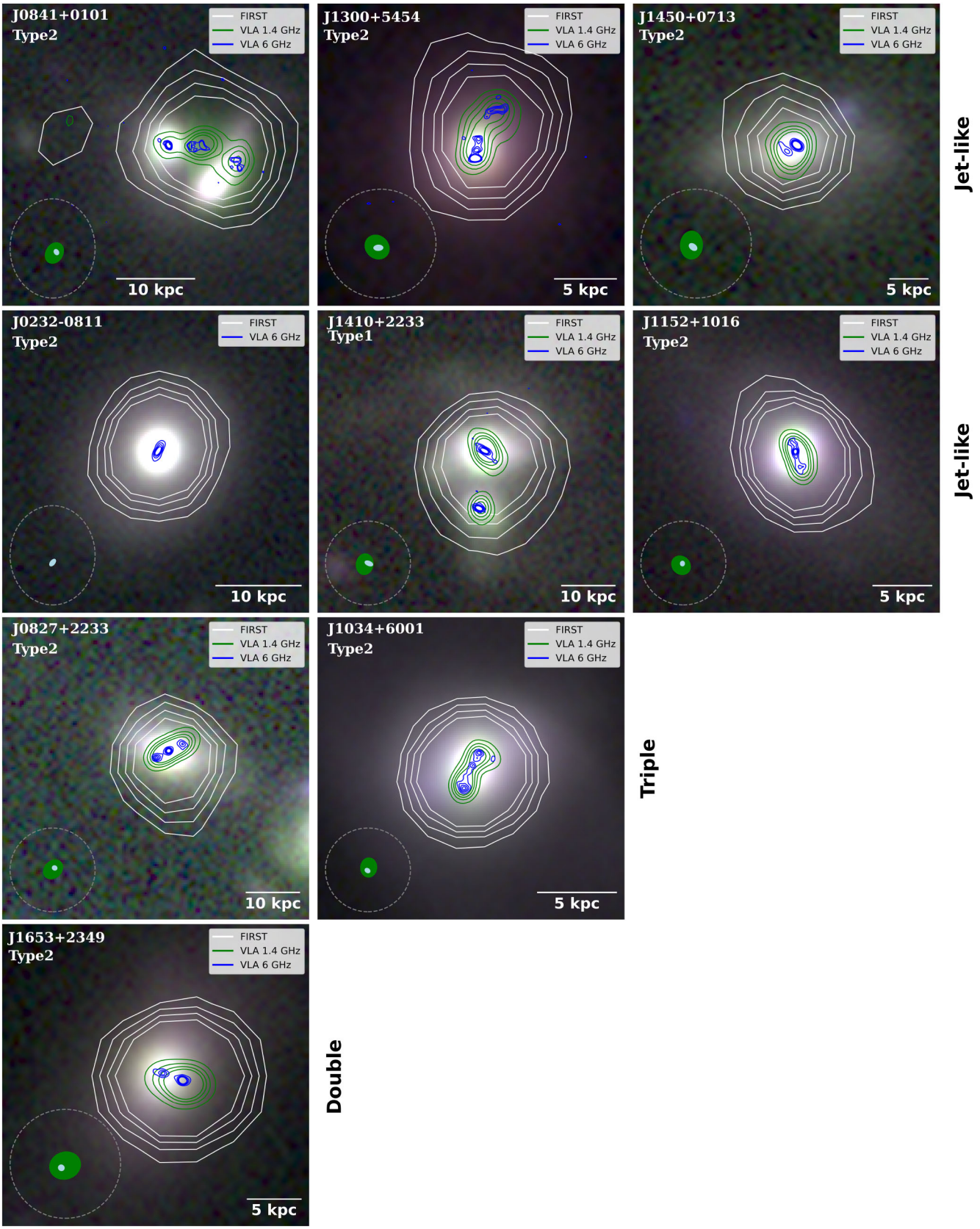

Figure 3. The same as Fig. 2, but presenting the nine targets identified as having extended 'jet-like' structures. These targets are classified as radio AGNs based on radio morphology. We note that the target J0232−0811 was not observed in the *L* band.

Downloaded from https://academic.oup.com/mnras/article/546/4/stag097/8427327 by University of Hertfordshire user on 18 February 2026

Table 2. The derived radio properties for the 29 QFeedS-2 targets, including multiple radio components per source when relevant. The columns are as follows: Column (1) gives the source ID. Columns (2) and (3) give the source positions from *C*-band data in J2000. Columns (4) and (5) give the total flux density and the peak brightness from the *L*-band maps. Column (6) is the LLS, derived from the *L* band; Column (7) gives the integrated flux ratios (R) between our *L* band and FIRST data; Columns (8) and (9) give the total flux density and peak brightness for the components observed in the *C*-band maps. Column (10) is the de-convolved linear size from the fits to the components observed in the *C*-band data (Section 3). Column (11) is the core spectral index (α, over 5.25–7.20 GHz; Section 4.3). Column (12) is the brightness temperature of the cores (Section 4.4). Column (13) is the radio morphology from visual inspection (Section 4.1). Column (14) highlights the sources classified as a radio AGN (Section 4.5). N/O indicates that the target was not observed in *L* band.

Source ID	RA	Dec.	$S_{1.4\,\mathrm{GHz}}$ (mJy)	$P_{1.4\,\mathrm{GHz}}$ (mJy beam^{-1})	LLS size(kpc)	$S_{1.4\,\mathrm{GHz}}/S_{\mathrm{FIRST}}$	$S_{6.3\,\mathrm{GHz}}$ (mJy)	$P_{6.3\,\mathrm{GHz}}$ (mJy beam^{-1})	Component (kpc)	SI α	log(T_{B}) (K)	Radio Morph.	Class
(1)	(2)	(3)	(4)	(5)	(6)	(7)	(8)	(9)	(10)	(11)	(12)	(13)	(14)
J0213+0042	02:13:59.79	+00:42:26.75	N/O	N/O	N/O	N/O	0.83±0.01	0.69±0.01	0.54±0.05	−0.71±0.15	2.95	Compact	
J0232−0811	02:32:24.25	−08:11:40.19	N/O	N/O	N/O	N/O	1.14±0.07	0.55±0.02	1.30±0.11	−1.36±0.37	2.11	Jet-like	R-AGN
J0827+2233	08:27:11.22	+22:33:24.21	2.48±0.12	1.25±0.04	6.35±0.40	1.22±0.10	0.27±0.01	0.20±0.01	5.0±0.07	−2.15±0.74	2.48	Triple	R-AGN
	08:27:11.27	+22:33:24.76	–	–	–	–	0.25±0.01	0.14±0.01	0.96±0.07	−1.07±0.36	1.74	–	–
	08:27:11.16	+22:33:24.64	–	–	–	–	0.21±0.01	0.1±0.002	1.12±0.05	−1.15±0.30	1.44	–	–
J0841+0101	08:41:35.08	+01:01:56.20	3.65±0.58	0.68±0.09	19.50±0.06	1.04±0.17	0.26±0.01	0.19±0.01	0.54±0.07	−0.91±0.94	2.16	Jet-like	R-AGN
J0924+1504	09:24:35.35	+15:04:10.00	2.71±0.09	2.33±0.04	1.50±0.13	0.79±0.03	0.65±0.02	0.51±0.08	0.48±0.03	−1.19±0.27	3.0	Compact	
J0947+1005	09:47:33.22	+10:05:08.75	1.31±0.07	1.06±0.04	1.63±0.36	0.93±0.08	0.47±0.01	0.46±0.01	< 0.80	−1.15±0.20	2.21	Compact	
J1034+6001	10:34:08.52	+60:01:53.00	17.60±2.40	5.41±0.57	3.28±0.52	0.93±0.13	1.72±0.12	0.57±0.03	2.54±0.05	−1.56±0.36	1.95	Triple	R-AGN
	10:34:08.577	+60.01.52.159	–	–	–	–	0.85±0.07	0.46±0.03	0.32±0.06	−1.36±0.26	2.27	–	–
	10:34:08.65	+60:01:50.72	–	–	–	–	0.51±0.01	0.39±0.06	0.20±0.01	−1.43±0.22	2.7	–	–
J1110+5848	11:10:15.24	+58:48:46.02	4.61±0.05	4.55±0.03	0.47±0.17	1.12±0.06	1.46±0.02	1.33±0.01	0.31±0.03	−1.17±0.12	3.67	Compact	
J1141+2156	11:41:16.16	+21:56:21.67	0.92±0.10	0.52±0.04	1.53±0.24	0.34±0.07	0.39±0.01	0.35±0.01	0.14±0.03	−0.86±0.66	3.11	Compact	
J1152+1016	11:52:45.66	+10:16:23.83	3.50±0.18	1.81±0.06	2.69±0.12	1.0±0.06	0.44±0.02	0.27±0.08	0.42±0.03	−1.06±0.52	2.24	Jet-like	R-AGN
J1203+1624	12:03:00.20	+16:24:43.72	3.01±0.04	2.66±0.02	1.67±0.08	1.04±0.05	0.83±0.02	0.57±0.01	0.87±0.03	−1.13±0.16	3.02	Compact	
J1300+5454	13:00:38.11	+54:54:36.39	2.61±0.34	0.70±0.07	5.64±0.8	1.21±0.17	0.14±0.06	0.12±0.01	0.24±0.09	−2.61±1.46	2.3	Jet-like	R-AGN
J1316+4452	13:16:39.75	+44:52:35.03	3.06±0.15	2.42±0.07	1.02±0.17	0.71±0.04	0.93±0.02	0.81±0.01	0.34±0.03	−1.13±0.18	3.11	Compact	
J1325+1137	13:25:52.16	+11:37:09.79	3.14±0.08	2.76±0.04	1.31±0.21	1.11±0.05	0.79±0.01	0.68±0.01	0.49±0.02	−0.97±0.18	3.7	Compact	
J1338+1503	13:38:06.53	+15:03:56.07	2.16±0.04	1.93±0.02	1.39±0.17	0.97±0.04	0.52±0.01	0.38±0.01	0.68±0.04	−1.19±0.21	2.68	Compact	
J1355+5612	13:55:16.56	+56:12:44.56	5.84±0.09	5.51±0.05	0.73±0.16	0.97±0.03	1.74±0.02	1.42±0.01	0.42±0.02	−0.97±0.12	3.4	Compact	
J1410+2233	14:10:41.51	+22:33:37.10	1.87±0.09	1.16±0.04	4.27±0.30	0.60±0.05	0.38±0.02	0.23±0.10	1.61±0.18	−1.9±0.20	1.98	Jet-like	R-AGN
J1419+1144	14:19:43.79	+11:44:26.24	2.49±0.04	2.26±0.02	1.13±0.08	0.85±0.04	0.75±0.02	0.52±0.01	0.79±0.07	−1.15±0.34	2.5	Compact	
J1426+1040	14:26:14.62	+10:40:12.86	2.16±0.06	1.72±0.03	1.74±0.20	1.10±0.07	0.58±0.02	0.46±0.01	0.48±0.08	−1.19±0.27	2.62	Compact	
J1426+1949	14:26:26.93	+19:49:54.22	1.81±0.03	1.66±0.02	1.42±0.17	1.57±0.08	1.7±0.01	1.66±0.01	0.19±0.02	−0.4±0.06	4.25	Compact	R-AGN
J1434+5016	14:34:11.19	+50:16:40.78	3.15±0.03	2.99±0.02	1.04±0.09	1.14±0.06	0.53±0.01	0.46±0.01	0.58±0.03	−1.97±0.37	3.41	Compact	
J1440+5303	14:40:38.20	+53:30:15.92	59.0±1.20	52.05±0.65	0.36±0.05	1.0±0.02	17.34±0.45	14.81±0.23	0.12±0.01	−0.93±0.02	4.49	Compact	
J1450+0713	14:50:34.10	+07:31:32.48	1.81±0.07	1.26±0.03	2.40±0.29	1.06±0.17	0.51±0.04	0.48±0.02	0.25±0.22	−1.13±0.45	3.38	Jet-like	R-AGN
J1507+0029	15:07:19.93	+00:29:04.95	4.40±0.05	4.39±0.03	0.88±0.08	1.0±0.03	1.14±0.05	0.82±0.02	0.88±0.08	−1.17±0.28	3.35	Compact	
J1529+5616	15:29:07.45	+56:16:06.67	4.45±0.14	3.90±0.08	0.91±0.22	1.04±0.05	1.19±0.03	0.9±0.02	0.35±0.03	−1.06±0.17	2.99	Compact	
J1543+1148	15:43:03.83	+11:48:38.45	2.72±0.03	2.65±0.02	0.53±0.11	1.30±0.07	0.88±0.01	0.73±0.01	0.36±0.14	−0.94±0.17	3.18	Compact	
J1653+2349	16:53:14.99	+23:49:42.55	6.81±0.31	5.14±0.15	2.41±0.22	0.95±0.05	1.28±0.06	0.90±0.03	2.09±0.04	−0.35±0.34	3.0	Double	R-AGN
	16:53:15:06	+23:49:42.91	–	–	–	–	0.68±0.07	0.32±0.02	0.91±0.11	−0.71±0.22	2.15	–	–
J1713+5729	17:13:50.31	+57:29:54.92	7.39±0.11	6.72±0.06	0.85±0.12	1.0±0.02	1.74±0.03	1.60±0.02	0.27±0.05	−1.34±0.19	3.77	Compact	
J2304−0841	23:04:43.48	−08:41:08.65	N/O	N/O	N/O	N/O	13.25±0.23	12.88±0.13	0.06±0.02	0.64±0.02	5.3	Compact	R-AGN

Downloaded from https://academic.oup.com/mnras/article/546/4/stag097/8427327 by University of Hertfordshire user on 18 February 2026

in Table 2. The ratios of integrated flux between our *L*-band maps and FIRST range from 0.34 to 1.57 with a median value of ∼ 1.0. Values of $R < 1$ indicate cases where FIRST records more integrated flux than our high-resolution *L*-band maps, which is consistent with diffuse emission resolved out by the higher resolution observations. We only find 5/26 of the sources (J1141+2156, J1410+2233, J1316+4452, J0924+1504, and J1419+1144, i.e. 19 per cent of the sample) have $R < 1$ values ($R = 0.34 - 0.85$) beyond the uncertainties. In all of these cases the *R* values are smaller than $R = 1$ at a significance that is greater than three times the uncertainties. In one of these cases, J1410+2233, the difference can be attributed to the secondary optical source in the field, which contaminates the FIRST flux. Therefore, only the remaining four cases show strong evidence that ≈15–66 per cent of the 1.4 GHz flux density is resolved out in our *L*-band maps. These results indicate that our *L*-band imaging recovers the bulk of the 1.4 GHz emission measured by FIRST for the large majority of the sample.

Conversely, $R > 1$ values indicate that our *L*-band maps contain more flux than measured by FIRST. This might indicate source variability between FIRST and our observations, minor variations due to slightly different frequency coverage, or other calibration and systematic errors (e.g. W. H. Vries et al. 2004; E. O. Ofek & D. A. Frail 2011; R. A. Perley & B. J. Butler 2013; K. P. Mooley et al. 2016; J. F. Radcliffe et al. 2019). We find 8/26 sources (J0827+2233, J1110+5848, J1300+5454, J1325+1137, J1426+1040, J1426+1949, J1434+5016, and J1543+1148; $R =$ 1.10–1.57) have values of $R > 1$ beyond the uncertainties. However, in all but two of these cases the differences are consistent with $R > 1$ only at three times the errors. Therefore, there is only weak evidence for values of $R > 1$ and we cannot rule out potential calibration/measurement issues. For the remaining two sources (J1426+1949 and J1543+1148, with R=1.57±0.08 and R=1.30±0.07, respectively) there may have been variability of the sources between the two observing epochs at the ∼30–60 per cent level.

We stress that additional causes, particularly time variability (FIRST epochs are typically years earlier than our new observations), different flux-extraction methods, and small frequency offsets combined with spectral curvature, can all produce deviations from $R = 1$. We therefore treat this comparison only as a rough indicator that, for the majority of our sources, there is not a significant fraction of large-scale gigahertz emission, which is missed by our *L*-band VLA observations. Single-dish data or lower frequency radio observations could better quantify any additional large-scale diffuse components missed by our observations (e.g. J. J. Condon 1992; L. E. H. Godfrey & S. S. Shabala 2016; L. K. Morabito et al. 2022).

4.2 Largest linear sizes in the radio

To estimate the radio LLS of each quasar, we used the *L*-band images under the assumption that the detected radio emission is fully confined within the *L*-band restoring beam. For compact sources, the LLS was taken directly from the deconvolved FWHM of the major axis returned by the two-dimensional Gaussian fitting performed with the CASA task IMFIT. These values are presented in Table 2. The quoted uncertainties correspond to the formal IMFIT errors on the deconvolved major axis; these incorporate the statistical uncertainties from the fit but do not explicitly propagate additional uncertainties in the restoring beam size and shape, potentially resulting in a underestimate of the true uncertainties.[5]

For sources exhibiting multiple components or clearly extended structures in the *L*-band images, we adopted the same LLS fitting procedure as M. E. Jarvis et al. (2021). In this approach, the LLS is defined as the projected separation between the outermost significant radio peaks. These peaks are identified in the cleaned image using intensity thresholds matched to the local rms, and their angular separation is converted to a linear scale using the source redshift. M. E. Jarvis et al. (2021) demonstrated that this method robustly captures the extent of jets, lobes, or knotty emission even when the morphology departs from a simple Gaussian and when individual components cannot be well-described by single-component fits. In cases where we detected a secondary radio component coincident with an optical galaxy (J0213+0042 and J1410+2233), we interpreted that component as an unrelated companion galaxy (see Section 4.1). Therefore, these secondary components were excluded from our LLS analysis. For the primary quasar component in these two systems, the LLS was taken from the deconvolved major-axis FWHM provided by CASA task IMFIT (as decribed above).

For the three targets (J0213+0042, J0232−0811, and J2304−0841) that were not observed in *L* band, we were forced to consider the IMFIT deconvolved major axis in *C* band as the LLS for these targets.

In Fig. 4, we plot $L_{1.4\,\mathrm{GHz}}$ (derived from the NVSS measurements) as a function of the LLS for the whole QFeedS sample, where the new QFeedS-2 sample is represented with green stars, and QFeedS-1 with black stars. The LLS values of QFeedS-2 range from 0.4 to 6.4 kpc, with two outliers at ∼0.1 kpc (J2304−0841; but we note that this is missing the *L*-band data) and ∼20 kpc (J0841+0101; see Fig. 3). Our new results reveal that the gigahertz radio emission is typically compact on host galaxy scales, i.e. confined within a few kiloparsecs. Indeed, visual inspection of the radio images shows that the radio emission is confined to the spatial extent of the optical emission (with the exception of J0841+0101).

The QFeedS-2 sources have a very similar distribution of LLS sizes to the majority of QFeedS-1 (see Fig. 4). The exception is that 10 (i.e. 24 per cent) of the QFeedS-1 sources have LLS values $\gtrsim$10 kpc, with only one source (i.e. 3 per cent) of QFeedS-2 reaching these scales. The QFeedS-1 targets with the largest sizes also tend to be those with the highest luminosities, i.e. $L_{1.4\,\mathrm{GHz}} \gtrsim 10^{24}\,\mathrm{W\,Hz^{-1}}$. We cannot rule out that even deeper radio observations would reveal lower surface brightness extended structures. However, for the majority of our sample the detected radio luminosity is dominated by the compact components recovered in our *L*-band maps.

[5]CASA IMFIT computes uncertainties on the deconvolved Gaussian parameters by propagating the covariance matrix of the best-fitting convolved model. The reported errors reflect statistical uncertainties from the fit (including pixel noise and parameter covariances), but they do not explicitly include systematic uncertainties due to the restoring beam model, residual calibration errors, or departures from a true Gaussian source structure. As a result, deconvolved sizes may have small formal uncertainties even when the intrinsic source size is smaller than the beam (see CASA Documentation: Image Analysis – IMFIT, CASA v6.5 from CASA Team 2022 and J. P. McMullin et al. 2007). However, IMFIT will not return a size measurement if the source cannot be de-convolved from the beam, and is consistent with an unresolved point source.

Downloaded from https://academic.oup.com/mnras/article/546/4/stag097/8427327 by University of Hertfordshire user on 18 February 2026

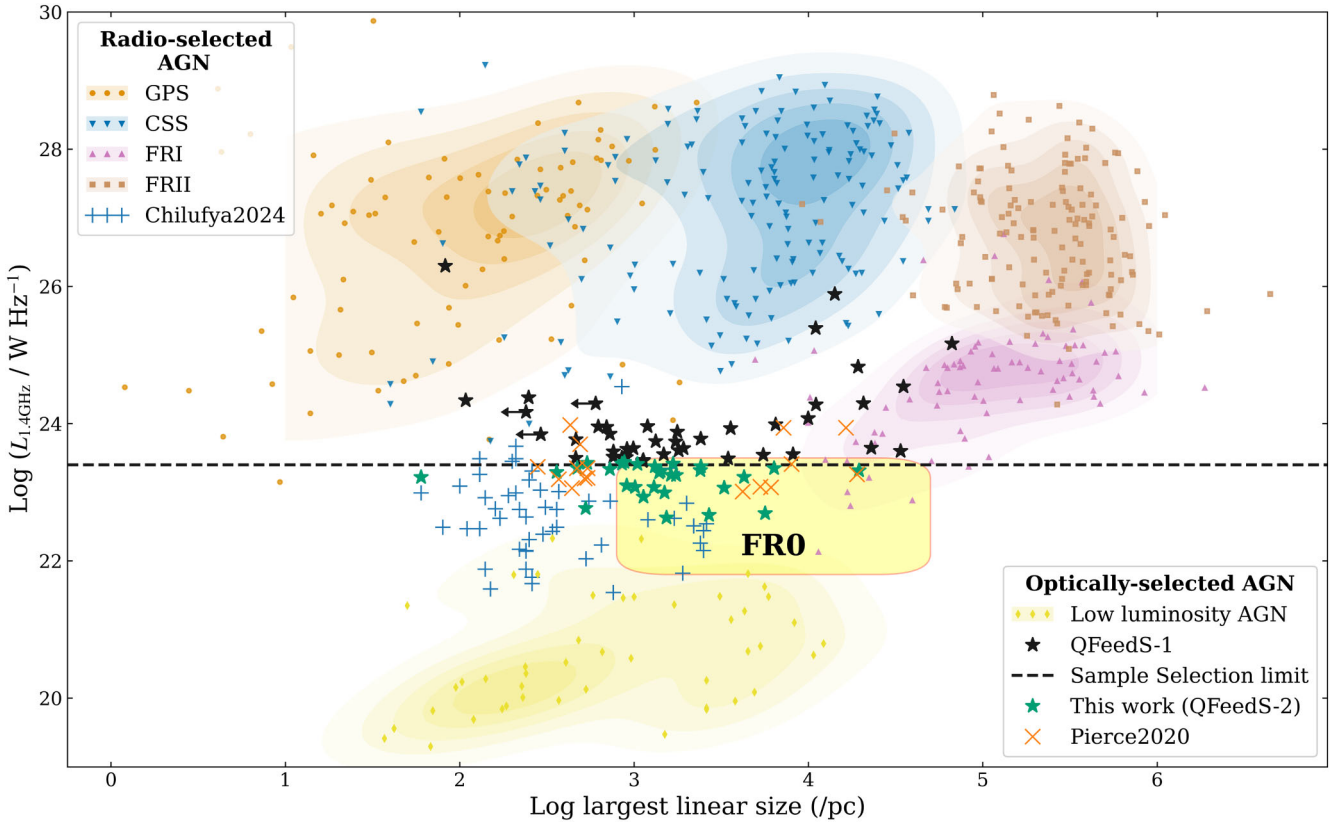

Figure 4. Radio size versus radio luminosity for the QFeedS quasars compared to classical radio-selected AGN populations. The coloured points and contours mark the loci of GPS, CSS, FRI, nad FRII sources, while the shaded yellow region highlights the FR0 domain as defined in R. D. Baldi (2023). The black stars show the QFeedS-1 sample (M. E. Jarvis et al. 2021), and the green stars show the new QFeedS-2 sample presented in this work. The dashed line marks the QFeedS-1 radio luminosity selection limit. The majority of QFeedS-2 remain compact at sub-arcsecond to arcsecond scales (~ 3 kpc), and broadly consistent with FR0-like systems. This distribution closely parallels the compact steep-spectrum sources reported in J. Chilufya et al. (2024) (plus symbols), though QFeedS quasars are optically selected and radiatively efficient, in contrast to many radio-selected samples. By contrast, QFeedS-1 shows a higher fraction of extended sources with higher radio luminosities, bridging towards CSS and FRI-like populations. At the same time, the QFeedS-2 sample overlaps in luminosity with the intermediate-power HERGs of J. C. S. Pierce, C. N. Tadhunter & R. Morganti (2020) (cross symbols), but stands out for its strong [O III] emission despite compact radio morphologies. Taken together, QFeedS maps a broad continuum of radio properties in optically selected quasars and highlights the role of QFeedS in connecting low-luminosity FR0-like AGNs with the more extended radio populations, while demonstrating the diversity of radio output among radiatively efficient quasars across several orders of magnitude in $L_{1.4\,\mathrm{GHz}}$.

This result highlights a limitation of wide low-resolution surveys such as FIRST, with a beam of ~ 5.0 arcsec, they cannot resolve the sub-kpc to few-kpc structures revealed by higher resolution VLA imaging. Indeed, all QFeedS-2 targets remained compact, i.e. without any visibly extended radio features in FIRST (except a marginal detection of a secondary component in J0841+0101; see top-left of Fig. 3). Our sensitive and high spatial resolution radio imaging shows that the radio emission is generally confined to the optical extent of the host galaxy, and that FIRST therefore often blends compact cores, small jets, and nearby companions into a single unresolved detection. Consequently, FIRST-scale surveys do not fully characterize the key spatial scales of radio activity in these radio-quiet quasars, and, therefore sensitive sub-arcsecond imaging is required to separate compact AGN components from genuinely diffuse emission and to robustly interpret the physical origin of the radio emission. In Section 5.3 we discuss QFeedS in the context of the other AGN populations presented in Fig. 4.

4.3 Spectral indices

Spectral indices provide a powerful diagnostic tool for identifying AGN cores, lobes, jets, and studying AGN feedback and lifecycles (e.g. R. A. Laing & J. A. Peacock 1980; M. C. Begelman, R. D. Blandford & M. J. Rees 1984; M. J. Hardcastle & J. H. Croston 2020; J. J. Harwood et al. 2022). Extragalactic radio sources follow the power-law spectra where the observed flux density follows $S_\nu \propto \nu^\alpha$. A flat or inverted spectrum $\alpha \geq -0.5$ is indicative of an AGN core and a steep spectrum $-0.5 \leq \alpha \lesssim -2$ is indicative of large scale emission from processes such as jets, lobes, shocks from outflows, and diffuse emission from star formation.

We measured the spectral index of radio cores identified in our *C*-band radio maps (5.25 − 7.20 GHz; see Section 3). For the multicomponent sources, the brightest radio peak was taken to be the core (although not necessarily a true 'core'). The spectral indices are listed in Table 2 and are presented in Fig. 5.

Only 3/29 (J1426+1949, J1653+2349, and J2304−0841), i.e. 10 per cent, of the QFeedS-2 targets show a flat spectrum ($\alpha \geq -0.5$). In comparison, 7/42 showed a flat spectrum (i.e. 17 per

Downloaded from https://academic.oup.com/mnras/article/546/4/stag097/8427327 by University of Hertfordshire user on 18 February 2026

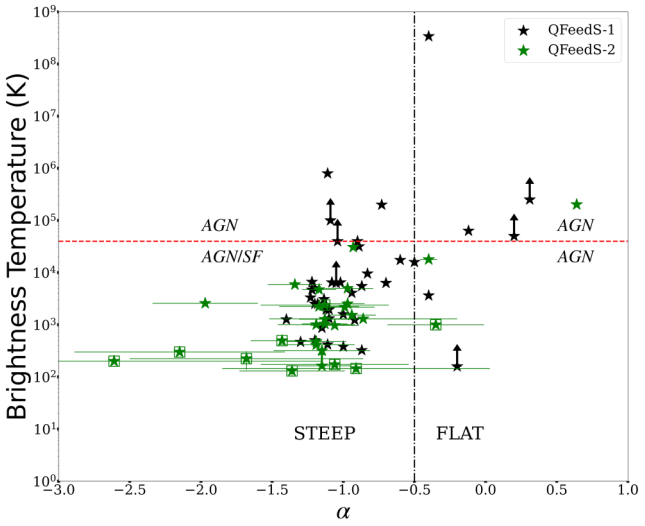

Figure 5. Brightness temperature (T_B) as a function of spectral index, α, (∼5–7 GHz) for the whole QFeedS sample. The black stars highlight the QFeedS-1 sample of 42 targets as presented in M. E. Jarvis et al. (2021). The new sample of 29 targets presented in this work (QFeedS-2) is highlighted by green stars. For the multicomponent sources, we plotted the component with the highest T_B value. The dashed red line highlights the lower limit of brightness temperature $T_B = 10^{4.6}$ K for selected radio AGNs. The vertical dot–dashed line separates flat and steep sources. For sources in the bottom-left quadrant, these radio measurements cannot distinguish between AGNs and star formation (SF). However, the targets highlighted by green squares indicate the QFeedS-2 sources that were classified as radio AGNs based on their morphology (Section 4.1).

cent) in the QFeedS-1 sample (M. E. Jarvis et al. 2021). Overall, only a minority of the sources (14 per cent) across the whole of QFeedS show flat or inverted cores (see Fig. 5). Indeed, the majority show very steep spectra with values around −1. The relevance of these measurements across the combined samples is discussed further in Section 5.1.

4.4 Brightness temperature

Brightness temperature (T_B) is defined as the temperature of a blackbody that would produce the observed radio surface brightness (flux density per solid angle) at the given frequency (e.g. L. K. Morabito et al. 2022). In practice, T_B serves as a proxy for radio surface brightness, whereby compact synchrotron-emitting AGN cores (the bases of jets) often show very high T_B because a large flux density is concentrated into a very small solid angle. By contrast, purely star-forming regions have a physical limit on the radio surface brightness they can produce. In fact, models of compact starbursts predict an upper bound of order $T_B \sim 10^5$ K even in the most extreme systems (J. J. Condon 1992). Thus, any unresolved radio core with a measured T_B above this starburst limit is a strong indicator of AGN activity.

To derive the brightness temperatures, we use our measurements from the high-resolution *C*-band data ($\theta_{res} \sim 0''.3$) and apply the standard equation (e.g. J. J. Condon et al. 1982; J. S. Ulvestad, R. R. J. Antonucci & R. Barvainis 2005; A. Njeri et al. 2025) as follows:

$$T_B = 1.22 \times 10^{12}(1+z)\left(\frac{S_\nu}{1\,\mathrm{Jy}}\right)\left(\frac{\nu}{1\,\mathrm{GHz}}\right)^{-2}\left(\frac{\theta_{maj}\theta_{min}}{1\,\mathrm{mas}^2}\right)^{-1}\ \mathrm{K}, \quad (2)$$

where θ_{maj} and θ_{min} are the deconvolved major and minor axes from the elliptical Gaussian model, S_ν is the observed peak flux density, and ν is the observing frequency. As noted by L. K. Morabito et al. (2022), this means T_B depends inversely on the observing frequency and beam size: at lower frequencies or higher resolution, the same flux density corresponds to a higher T_B. Using our ∼ 0.3 arcsec beam at ∼ 6 GHz (Equation 2), we derive T_B for each source. These values are presented in Fig. 5 and are tabulated in Table 2.

To distinguish AGNs from star formation, we adopt the same criteria used by M. E. Jarvis et al. (2021), namely $T_B > 10^{4.6}$ K. M. E. Jarvis et al. derive this threshold by scaling the J. J. Condon et al. (1991) starburst limit to *C* band. At our central frequency of ∼ 6 GHz and redshift ($z \sim 0.1$), starbursts are not expected to exceed this value, so any brighter core is expected to be AGN-dominated. The T_B values for the QFeedS-2 sample range from 1.3×10^2 to 2.0×10^5 K, with only one target (i.e. ∼ 3 per cent), J2304−0841, meeting this criterion (see Fig. 5). For comparison, about ∼ 17 per cent of the QFeedS-1 cores exceed $10^{4.6}$ K (black stars in Fig. 5), reflecting that those sources are on average more radio-luminous and host more compact high T_B cores.

It is important to note that T_B is a very conservative radio-AGN diagnostic and a measurement below $T_B < 10^{4.6}$ K does not prove the absence of a radio emission associated with AGNs. Many QFeedS-2 sources have lower peak fluxes and slightly resolved low-surface brightness cores, which lead to beam dilution and thus could underestimate the T_B measurements. Additionally, T_B measurements depend strongly on the resolution and can underestimate T_B for extended or partially resolved sources, potentially missing the weaker AGN cores (e.g. J. F. Radcliffe et al. 2018; L. K. Morabito et al. 2022, 2025b; A. Njeri et al. 2023, 2025). Indeed, high spatial resolution and high sensitive radio imaging can be more effective at isolating true AGN cores, with high T_B, from dilution from other processes (see discussion of QFeedS-1 using higher resolution radio data in A. Njeri et al. 2025). In general, one can only securely classify a source as AGN if T_B exceeds the starburst limit (e.g. L. J. Kewley et al. 2000). If T_B is below the limit, the source may still host an AGN core, but any bright AGN contribution would need confirmation via other means (see 'AGN/SF' region in Fig. 5). For this reason, we use T_B as one diagnostic among several. As in previous work, we supplement this diagnostic with spectral index and morphology diagnostics to identify AGN-related radio emission (M. E. Jarvis et al. 2019; A. Njeri et al. 2025). As discussed in the following sub-section, this multicriteria approach is essential for identifying radio emission associated with AGNs.

4.5 Radio-AGN identification

No QFeedS-2 target is classified as 'radio loud' based either on their radio to [O III] luminosities (applicable for all sources) or radio to optical continuum luminosities (applicable for the Type 1 sources; see Section 2.3). Radio-quiet quasars exhibit radio luminosities that are orders of magnitude fainter than their radio-loud counterparts, typically in the range $L_{1.4\,\mathrm{GHz}} \sim 10^{21-25}\,\mathrm{W\,Hz^{-1}}$ (N. L. Zakamska et al. 2004; P. Padovani 2016). These faint signals are easily lost due to sensitivity limitations, or could be overwhelmed by star formation contributions, especially in shallow or low-resolution surveys such as NVSS or FIRST. Thus, detecting and characterizing radio emission from radio-quiet quasars is extremely challenging. Using sensitive high-resolution radio imaging obtained in this work, we probed for the presence of radio

Downloaded from https://academic.oup.com/mnras/article/546/4/stag097/8427327 by University of Hertfordshire user on 18 February 2026

emission associated with AGN based on the radio morphology (Section 4.1), the spectral index (Section 4.3), and the brightness temperature (Section 4.4):

(i) Radio morphology: high-resolution radio imaging can identify structures on a few kiloparsec to sub-kiloparsec scales. Elongated emission, double-lobed structures, well-collimated multiple components, and linear features extending from a central source are indicative of low-power AGN jets, possibly compact due to confinement or young age, or from shocks caused by quasar winds (e.g. J. Nims et al. 2015; R. D. Baldi, G. Giovannini & A. Capetti 2021; A. Njeri et al. 2025). Nine targets (i.e. ~ 31 per cent) show such morphologies (see Fig. 3) and are therefore classified as radio AGNs.

(ii) Spectral indices: our high-resolution radio imaging enabled us to identify compact nuclear components of these radio-quiet quasars targets. Three targets (J1426+1949, J1653+2349, and J2304−0841, i.e. ~ 10 per cent) show a flat spectrum ($\alpha \geq -0.5$), which is likely indicative of an AGN 'core', and are therefore classified as radio AGNs. One of these sources, J1653+2349, is already considered a radio AGN based on morphology.

(iii) Brightness temperature ($T_{\rm B}$): high $T_{\rm B}$ values are inconsistent with star formation and point to synchrotron emission from an AGN core (e.g. J. J. Condon 1992). A compact unresolved radio core at sub-arcsecond (< 0.3 arcsec) scales with high $T_{\rm B} > 10^{4.6}$ K is indicative of radio AGNs. Only one target (J2304-0841; i.e. ~ 3 per cent) has $T_{\rm B} > 10^{4.6}$ K. This target was already considered a radio AGN based on a flat spectral index.

Overall, 11/29 targets (~ 38 per cent) of QFeedS-2 are classified as radio AGNs using the combined criteria of radio morphology, spectral index, and brightness temperature. However, the origin of radio emission in the remaining 18/29 (~ 62 per cent) remains uncertain, largely due to our radio data limitations and a lack of complementary multiwavelength data, particularly in the far infrared. For example, with far infrared emission we could assess if the radio luminosity is above that expected from star formation following the far-infrared radio correlation of star-forming galaxies (e.g. A. Del Moro et al. 2013; J. Delhaize et al. 2017; M. E. Jarvis et al. 2021; Y. Wang et al. 2024; J.-M. Eberhard et al. 2025, also see Section 5.2.1). Therefore, we consider the 38 per cent of radio-identified AGNs in QFeedS-2 to be a lower limit of the true fraction.

5 DISCUSSION

The full QFeedS comprises of 71 optically selected $z < 0.2$ quasars (Section 2.2). Combining the initial QFeedS-1 sample (M. E. Jarvis et al. 2021) and QFeedS-2 sample (this work), this spans an extensive radio luminosity range of $L_{1.4\,\rm GHz} = 10^{22.6}$–$10^{26.3}\,\rm W\,Hz^{-1}$, encompassing nearly four orders of magnitude. The QFeedS-1 sample covers the higher luminosities, with a radio luminosity range of $L_{1.4\,\rm GHz} = 10^{23.45}$–$10^{26.30}\,\rm W\,Hz^{-1}$ and a median of $\sim 10^{23.8}\,\rm W\,Hz^{-1}$, while the low-luminosity QFeedS-2 sample has a radio luminosity range of $L_{1.4\,\rm GHz} = 10^{22.63}$–$10^{23.44}\,\rm W\,Hz^{-1}$, and a median of $\sim 10^{23.29}\,\rm W\,Hz^{-1}$.

This combined sample enables a rare opportunity to systematically study how the radio emission in quasars evolves with radio luminosity, and obtain more insight into feedback processes in a representative quasar sample. Here we discuss the radio AGN identification across the full QFeedS sample (Section 5.1), before exploring more deeply the potential origins of the radio emission (Section 5.2), and comparing to other AGN populations (Section 5.3).

5.1 Radio-AGN identification in the full QFeedS sample

In Fig. 5, we summarize the radio-AGN selection criteria used in this work for QFeedS-2 (green stars), which are (1) morphology (highlighted with squares; nine targets, i.e. 31 per cent); (2) flat core spectral indices of $\alpha > -0.5$ (right of dot–dashed line; three targets, i.e. 10 per cent); and (3) high brightness temperature measurements (above horizontal dashed line; one target, i.e. 3 per cent). Based on these combined criteria, 11/29 (38 per cent) of sources are classified as radio AGNs in QFeedS-2. In the same figure we show QFeedS-1 (black stars), which show a higher incidence of flat spectral indices ($17^{+6.5}_{-5.0}$ per cent, compared to $10^{+7.0}_{-4.4}$ per cent in QFeedS-2) and high brightness temperatures ($17^{+6.5}_{-5.0}$ per cent compared to $3^{+5.2}_{-2.1}$ per cent in QFeedS-2).

Following the same radio morphology criteria applied in this work (i.e. sources with double, triple, or jet-like morphologies), $55^{+7.5}_{-7.7}$ per cent[6] of targets in the QFeedS-1 sample are classified as radio AGNs based on radio morphology alone, compared to $31^{+9.1}_{-7.8}$ per cent in QFeedS-2. These fractions of identified AGN-like morphologies are broadly consistent with results for comparable samples at similar luminosities and redshifts (see Section 5.3). The QFeedS-1 sources span radio sizes of ~ 0.1–67 kpc (M. E. Jarvis et al. 2021), while QFeedS-2 sizes range ~ 0.1–20 kpc (see Fig. 4). Most objects in both samples have radio emission confined to host-galaxy scales (i.e. $\leq$ a few kpc), although a minority of QFeedS-1 sources and one QFeedS-2 target exhibit substantially larger sizes (see Section 4.2). Importantly, this size distribution masks a wide variety of radio morphologies, and even though the targets were selected to have similar [O III] luminosities, we observe compact unresolved cores, small jets, hotspots, and diffuse structures across the whole sample (Figs 2 and 3).

Using the consistent and combined three criteria of radio morphology, brightness temperature, and spectral indices, we identify 28/42 ($67^{+6.8}_{-7.6}$ per cent) and 11/29 ($38^{+9.3}_{-8.5}$ per cent) sources as radio AGNs across QFeedS-1 and QFeedS-2, respectively. However, it is already known that additional information can identify more radio AGNs, and these are likely lower limits of the true fractions. For example, using sufficiently high-quality far-infrared measurements, which were available for a sub-set of the sample, M. E. Jarvis et al. (2021) found another 12 per cent of QFeedS-1 quasars to be classified as radio AGNs solely based on radio-excess measurements (following e.g. G. Helou, B. T. Soifer & M. Rowan-Robinson 1985; J. J. Condon 1992; A. Del Moro et al. 2013; J. Marvil, F. Owen & J. Eilek 2015), i.e. where their radio morphology, spectral indices, and brightness temperature criteria were inadequate (see fig. 6 in M. E. Jarvis et al. 2021). Sufficient quality far-infrared data are not available for QFeedS-2 for a comparable

[6]We note that 67 per cent of sources in M. E. Jarvis et al. (2021) are described as having extended structures. However, excluding sources showing diffuse/irregular morphologies, only 55 per cent of the sample is classified as radio AGNs based on morphology alone. We also note that M. E. Jarvis et al. (2021) quoted a lower fraction of ∼16 per cent based on much stricter morphology criteria; however, here we apply a looser criteria, following A. Njeri et al. (2025), and note that sources not classified as radio AGN based on morphology in M. E. Jarvis et al. (2021) are identified as radio AGN based on other diagnostics, reassuring us that this is a reasonable approach.

Downloaded from https://academic.oup.com/mnras/article/546/4/stag097/8427327 by University of Hertfordshire user on 18 February 2026

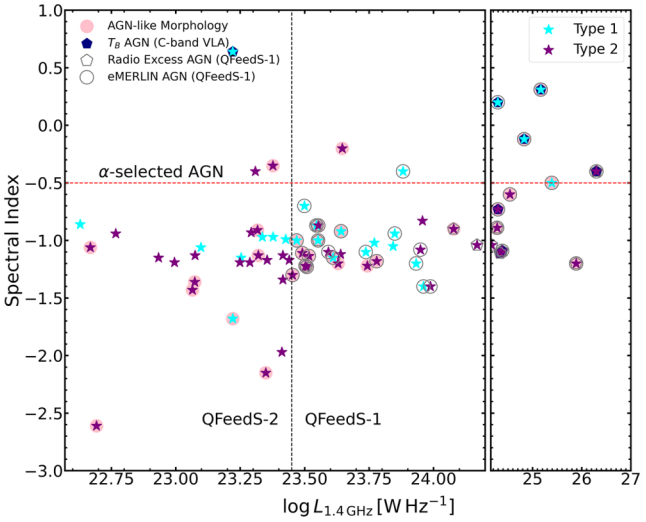

Figure 6. Core spectral index (∼5–7 GHz) versus 1.4 GHz (NVSS) radio luminosity for the QFeedS sample. The vertical dashed line separates QFeedS-1 from QFeedS-2 sources. The plot is split into two panels, covering different luminosity ranges for more clarity over the wide parameter space. The cyan stars denote Type 1 quasars and the purple stars denote Type 2 quasars. The solid circles highlight quasars identified as radio AGNs based on the criteria used in this work. Both sub-samples are dominated by steep spectrum emission; however, flatter-spectrum sources are more common at higher luminosities (QFeedS-1), for the Type 1 quasars, consistent with an increased contribution from compact AGN-related cores. The open circles mark QFeedS-1 sources identified as radio AGNs based on follow-up higher resolution *e*-MERLIN radio imaging.

analysis; however, we briefly investigate the likely contribution of star formation in Section 5.2.1. Overall, this highlights the need for high-resolution multiband radio imaging combined with multiwavelength information, particularly infrared, as we push further into the radio-quiet regime (also see e.g. M. J. Hardcastle et al. 2025).

In Fig. 6 we present a summary of the radio-AGN identification approaches across the whole QFeedS sample, in the form of spectral index versus radio luminosity diagram.[7] Unsurprisingly, for the moderate radio luminosities covered by the QFeedS quasars, only a minority of the sample have strong radio-AGN cores based on our VLA data, as indicated by flat spectral indices or high brightness temperatures. However, as expected, this fraction increases as a function of radio luminosity. On the other hand, radio morphology results in a higher fraction of radio AGNs being identified in QFeedS, which is only possible due to our high-resolution radio maps.

Higher resolution follow-up of QFeedS-2 is needed because a substantial fraction of the radio power in these quasars appears to arise on sub-kiloparsec scales (i.e. $\lesssim 1$ kpc to a few hundred parcecs; e.g. A. Njeri et al. 2025). Compact cores, frustrated jets, hotspot knots, and shocked regions can all be concentrated within these small spatial extents and therefore remain unresolved or beam-diluted in our VLA maps. Observations with finer angular resolution (e.g. *e*-MERLIN at ≤ 100 pc scales or VLBI at parsec scales) both increase brightness temperature sensitivity and resolve compact AGN features, often revealing AGN signatures missed at lower resolution. For example, 6 GHz *e*-MERLIN imaging of the QFeedS-1 sample at ≤ 100 pc resolution increases the fraction of sources confidently classified as radio AGNs to nearly 90 per cent (see open circles in Fig. 6), compared with 60 per cent identified from low-resolution data (A. Njeri et al. 2025). Higher resolution observations of QFeedS-2 are likely to uncover additional compact AGN components and to provide a more complete census of radio AGN across the full QFeedS luminosity range.

[7]One QFeedS-1 target (J1016+0028) is absent from Fig. 6 due to the lack of a core spectral index measurement, as it was undetected in the *C*-band data (M. E. Jarvis et al. 2021). Nevertheless, we note that the source was classified as a radio AGN based on its morphology.

5.1.1 *Type 1 versus Type 2 quasars*

Since our sample is composed of ~ 35 per cent Type 1 and ~ 65 per cent Type 2 quasars, we briefly investigate the radio properties across the two classes of AGNs in our QFeedS sample. The division of sources into optical Type 1 (cyan stars) and Type 2 (purple stars) in Fig. 6 shows no strong offset in spectral index distribution between the two classes. The exception is for the highest radio luminosities ($\gtrsim 10^{24}$ W Hz^{-1}), where the Type 1 systematically have flatter spectral indices. We also note that the extended AGN-like morphologies are more frequently identified in Type 2 sources, with ~ 52 per cent compared to only ~ 32 per cent for the Type 1. These trends, albeit weak, may reflect observational biases in detecting compact cores against different host galaxy environments (N. L. Zakamska et al. 2016; M. Villar Martín et al. 2021), and are broadly consistent with an orientation-based model. Specifically, for a more directly face on view for Type 1 quasars, we would expect the radio emission to be more dominated by the radio core (with compact flat-spectrum emission).

5.2 Potential origin of the radio emission

For ∼60 per cent of our QFeedS-2 sample, which covers the modest radio luminosities ($L_{1.4\,GHz} \sim 10^{22.63}$–$10^{23.45}$ W Hz^{-1}), the origin of the radio emission remains ambiguous. Although we lack the diagnostics to definitively rule out star formation in individual targets, here we briefly assess the likelihood that star formation is a dominantly contributing factor across the QFeedS sample as a whole.

5.2.1 *Star formation versus radio-quiet AGNs*

Single-band radio conversions have been used to convert radio luminosity into star formation rates for star-forming galaxies (e.g. M. S. Yun, N. A. Reddy & J. J. Condon 2001; E. J. Murphy et al. 2011; R. C. Kennicutt & N. J. Evans 2012). Compact low-power jets, wind–ISM shocks, and coronal synchrotron all produce steep-spectrum emission that masquerades as star formation when using single-band radio calibrations. Therefore, when AGNs may be present these calibrations would only provide upper limits on star formation rate measurements (e.g. M. S. Yun et al. 2001; A. Del Moro et al. 2013; P. Padovani 2017). Based on large sample studies, at $L_{1.4\,GHz} \approx 10^{23}$ W Hz^{-1}, the radio emission in quasars increasingly overlaps the regime of star-forming galaxies, with non star-forming processes easily supplying a large fraction of the radio power. We place our QFeedS sample into the context of such studies, assessing the likely contribution from star formation to the sample as a whole.

Downloaded from https://academic.oup.com/mnras/article/546/4/stag097/8427327 by University of Hertfordshire user on 18 February 2026

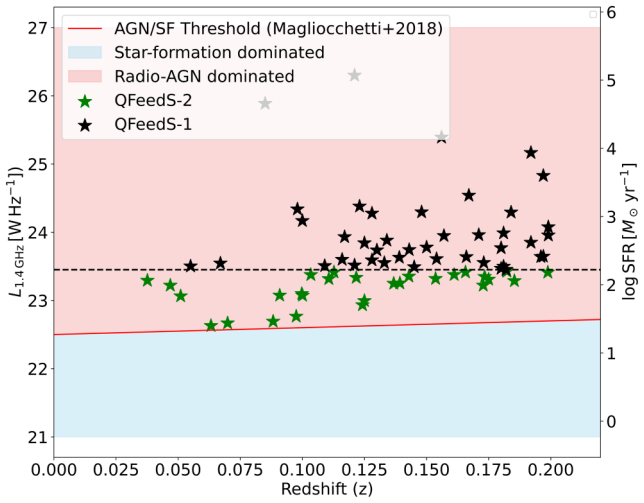

Figure 7. Radio luminosity at 1.4 GHz (NVSS) versus redshift for QFeedS quasars and the corresponding star formation rates as derived from the standard star formation rate calibrators is shown on the right axis (see Section 5.2.1). The black stars represent QFeedS-1 and green stars represent QFeedS-2. The solid red line shows the AGN/star formation threshold for the galaxy population from M. Magliocchetti et al. (2018), separating the star-formation-dominated (blue shaded) and radio-AGN-dominated (pink shaded) regimes. The dashed black line marks the QFeedS-1/QFeedS-2 selection limit. Most QFeedS quasars, particularly the luminous QFeedS-1, lie firmly above the star-forming locus, indicating that their radio emission is most likely dominated by AGN processes rather than star formation. The lower luminosity QFeedS-2 source scatter closer to the threshold but still occupy predominantly AGN-dominated space.

In Fig. 7 we present radio luminosity as a function of redshift for the combined QFeedS samples. As a rough estimate, on the right-hand axis, we convert these radio luminosities into star formation rates, assuming a 100 per cent contribution from star formation to the radio emission and averaging multiple conversion calibrations (M. S. Yun et al. 2001; E. J. Murphy et al. 2011; R. C. Kennicutt & N. J. Evans 2012). The inferred star formation rates range from ∼30 to ∼ 10^5 $M_\odot$ yr^{-1}. For context, the typical star formation rates of radiatively luminous AGNs at $z \sim 0$ are found to be 0.1–50 $M_\odot$ yr^{-1} (e.g. N. L. Zakamska et al. 2016; T. T. Shimizu et al. 2017; M. E. Jarvis et al. 2019; T. M. Jackson et al. 2020). Using this conversion, we find that 67/71 (94 per cent) of the inferred star formation rates are greater than 50 $M_\odot$ yr^{-1}, which is an uncomfortably high value for these very low-redshift quasars. Therefore, it is most likely that there is a significant contribution to the radio emission from AGNs for the majority of the sample. Indeed, these standard single-band calibrations yield implausibly high star formation rates in AGN hosts due to contamination from compact synchrotron processes. The inflated inferred star formation rate values we measure are consistent with previous works that report radio-based star formation rates in quasars and radio-quiet AGNs tend to overshoot far-infrared or spectral energy distribution based estimates due to contamination from low-power jets, coronal activity, and wind-driven shocks (e.g. A. Del Moro et al. 2013; E. Behar et al. 2015; N. L. Zakamska et al. 2016; I. Delvecchio et al. 2017; P. Padovani 2017; V. Smolčić et al. 2017; E. Bernhard et al. 2022; G. Calistro Rivera et al. 2024; M. Liao et al. 2024).

We further compare to the redshift-dependent separation between star-formation-dominated and AGN-dominated radio luminosity regimes as derived by M. Magliocchetti et al. (2018), which is represented by the solid red curve in Fig. 7. The QFeedS-1 quasars, at higher radio luminosities, sit firmly within the AGN-dominated region, consistent with their high fraction of radio AGN identification from other methods (M. E. Jarvis et al. 2021; A. Njeri et al. 2025). In contrast, QFeedS-2 sources cluster closer to the threshold, with some appearing near the boundary between the two regimes; however, still within the AGN-dominated regime.

Although we cannot rule out a significant contribution from star formation in all individual sources, we conclude that the QFeedS quasars, which are pre-selected as luminous [OIII] and radio detected in FIRST, are likely to have their radio emission predominantly associated with AGN-related processes. This supports the idea of an increasing body of work implying a significant contribution of AGN-related emission to the radio output of radio-quiet quasars (e.g. N. L. Zakamska et al. 2016; S. V. White et al. 2017; F. Panessa et al. 2019).

5.2.2 *Jets and winds in radio-quiet quasars*

At the high-luminosity end (QFeedS-1), the radio emission is often clearly AGN-dominated, with compact jet-like morphologies, flat to moderate spectral indices, and high brightness temperatures ($T_B \geq 10^{4.6}$ K), pointing to relativistic jet activity as the primary driver, although shocks due to quasar-driven winds cannot be ruled out in all cases (M. E. Jarvis et al. 2021). These sources align with classical radio-intermediate and radio-loud quasars, where radio-AGN activity is well established (M. E. Jarvis et al. 2021; A. Njeri et al. 2025).

Interestingly, the majority of QFeedS sources show very steep spectral indices of ≈−1 (Fig. 6). Such a steep spectral slope could be an indication of shocks due to quasar-driven winds and/or low power radio jets interacting with the ISM (e.g. C. P. O'Dea 1998; J. Nims et al. 2015; V. A. Fawcett et al. 2025). Indeed, spatially resolved multiwavelength analysis of subsets of the QFeedS-1 sample show a high incidence of interaction with the ISM (e.g. M. E. Jarvis et al. 2019; A. Girdhar et al. 2022, 2024). However, distinguishing between jets and winds as the origin of the radio emission in AGN-dominated systems is very challenging. While spatially resolved polarization-sensitive observations may provide some diagnostics, sensitivity-limited imaging alone can be expected to remain ambiguous based on simulations (e.g. M. Meenakshi et al. 2024). None the less, in sources where 'AGN-like' (extended) morphologies are observed in QFeedS-2 (see Fig. 3), we discuss their morphologies below, in the context of previous observations.

The jet-like feature in J0841+0101 appears to be bipolar with an end-to-end extent of nearly 20 kpc. It is important to note the filamentary nature of the jet and its western end lying close to the neighbouring galaxy (but not coincident with its optical centre). On the eastern end, only a single radio feature is observed, and only in the *L*-band data. The jet-like features in J1300+5454, J1034+6001, J0827+2233, and J1152+1016 display morphologies similar to those observed in jetted radio-loud AGNs except for the fact that these jets are much smaller in extent. J1300+5454, J1034+6001, and J0827+2233 appear to show terminal hotspots like FRII radio galaxies, while the jet in J1152+1016 shows an S-shaped FRI-like morphology. The more compact extensions in J0232−0811 and J1410+2233 resemble similar extensions observed in Seyfert galaxies and other radio-quiet quasars (e.g. V.

Downloaded from https://academic.oup.com/mnras/article/546/4/stag097/8427327 by University of Hertfordshire user on 18 February 2026

V. Rao et al. 2023; S. Silpa et al. 2023). The radio structures in J1450+0713 and J1653+2349 resemble a core-hotspot-like structure but the counter-hotspot is not clearly visible. For all radio sources that are compact (Fig. 2), it is possible that jets exist on even smaller sub-kpc scales that would need sub-arcsecond or VLBI observations to resolve (e.g. P. Kharb et al. 2019, 2021; A. Njeri et al. 2025).

Taken together, these diverse jet-like morphologies illustrate that even within radio-quiet quasars, small-scale jets and compact outflows significantly impact the observed radio emission. Although much smaller than classical FR I/II radio galaxies (Fig. 4), the presence of hotspots, bends, and filamentary features strongly suggests jet–ISM interactions, rather than star formation origins (e.g. R. D. Baldi et al. 2018; M. E. Jarvis et al. 2019; D. J. Rosario et al. 2020). At the same time, the coexistence of compact steep-spectrum sources without obvious extended features highlights that multiple mechanisms, ranging from low-power or frustrated jets, coronal emission, and outflow-driven shocks, likely contribute across the QFeedS population (e.g. A. Laor & E. Behar 2008; F. Panessa et al. 2019; S. Silpa et al. 2023). Thus, the radio emission in these quasars is unlikely to be ascribed to a single origin. Instead, it reflects a continuum of AGN-driven processes operating over different spatial and energetic scales, potentially intertwined with the dynamical state of the host galaxy (e.g. P. Padovani 2017; M. J. Hardcastle & J. H. Croston 2020).

5.3 Comparison to other AGN samples

Compact low-luminosity radio AGNs often exhibit steep spectra and show jet-like structures on kiloparsec (or smaller) scales, if spatially resolved (see review by R. D. Baldi 2023). For QFeedS-2, 26/29 sources show steep spectra $\alpha < -0.5$ (Fig. 5), consistent with optically thin synchrotron emission. However, since nearly all remain compact on kiloparsec scales, this compactness likely reflects low-power or frustrated jets, or shocks from quasar-driven winds, confined to small spatial scales (e.g. R. D. Baldi, A. Capetti & G. Giovannini 2015; S. Silpa et al. 2020; R. D. Baldi 2023; A. Njeri et al. 2025, Section 5.2.1). As shown in Fig. 4, the QFeedS quasars have radio sizes overlapping compact steep spectrum (CSS) and low-size end of FRI sources. Strikingly, $\sim$ 80 per cent of the QFeedS-2 sources cluster in the same region as FR0 galaxies (Fig. 4; yellow shaded region), which is traditionally associated with low-accretion radio galaxies (R. D. Baldi 2023). However, the high [O III] luminosities of our sample indicate radiatively efficient quasars, illustrating a decoupling between radiative accretion power and observed radio luminosities and sizes.

The compact low-luminosity objects in QFeedS may also represent early evolutionary stages of gigahertz peaked spectrum (GPS) and CSS sources, in which jets remain confined within their host galaxies (particularly for the QFeedS-1 sample; see more discussion in A. Njeri et al. 2025). M. Kunert-Bajraszewska et al. (2010) proposed that such low-luminosity compact systems could be young radio sources that later evolve into CSS of FRI galaxies, while M. M. Slob et al. (2022) similarly identified compact peaked-spectrum sources in LOFAR consistent with either young or confined jets.

Recent low-redshift studies provide additional insights into the low-luminosity compact radio AGN population. For instance, J. C. S. Pierce et al. (2020) analysed intermediate-power high-excitation radio galaxies (HERGs; $22.5 < \log L_{1.4\,\mathrm{GHz}} < 24.0\,\mathrm{W\,Hz^{-1}}$) at $z < 0.1$ and found a lower incidence of extended radio morphologies, steep-spectrum compact sources in the less powerful half of their sample, compared to classical radio galaxies (see crosses in Fig. 4). This may suggest that the low-power AGNs can persist in relatively undisturbed systems, contrasting with the merger-driven environments of more powerful radio AGNs. The QFeedS-2 sample, while overlapping in radio luminosity with these HERGS, they differ in that they are preselected as luminous [O III] quasars, pointing to strong radiative accretion event with radio output that is relatively compact and weak.

Similarly, J. Chilufya et al. (2024) studied LOFAR-selected low-luminosity ($L_{150\,\mathrm{MHz}} < 10^{25}\,\mathrm{W\,Hz^{-1}}$) radio AGNs at $0.03 < z < 0.1$ and reported that most sources are unresolved at sub-kpc scales, and often have steep-spectrum, strongly resembling CSS, GPS, and FR0-like systems (see plus symbols in Fig. 4). This is directly comparable to the QFeedS-2 sources, which also occupy the FR0 region in the luminosity–size plane. The strong overlap highlights that compact confined radio sources are common manifestation of low-radio power AGN activity across both radio-selected and optically selected samples. These comparisons underscore that the QFeedS sample maps on to the broader landscape of compact radio-AGN populations. While J. C. S. Pierce et al. highlight the role of host morphology, J. Chilufya et al. emphasize the compactness and FR0-like character, with the QFeedS connecting these with the quasar regime of high radiative accretion, demonstrating how luminous quasars can host radio emission that mimics low-power radio galaxies. Overall, the QFeedS sample traces a continuum, from luminous quasars with extended jet-like structures to compact low-power systems whose radio emission resembles FR0s, thereby mapping the diversity of radio AGN activity across nearly four orders of magnitude in radio luminosity.

6 CONCLUSION

We present a new sample of 29 $z < 0.2$ quasars (QFeedS-2) with $L_{1.4\mathrm{GHz}} < 10^{23.45}\,\mathrm{W\,Hz^{-1}}$, as an extension to our QFeedS (see Fig. 1). In this work, we study the gigahertz radio emission using new 1.4 GHz (L-band) and 6 GHz (C-band) data from the VLA, which cover a spatial resolution of $\sim$ 1–3 kpc. Our main conclusions are as follows:

(i) For the vast majority of sources ($\sim$ 80 per cent), our L-band VLA imaging recovers the FIRST 1.4 GHz flux, indicating that the high-resolution maps capture the bulk of the total gigahertz emission.

(ii) The gigahertz radio emission is extended on $\sim$0.1–20 kpc scales. $31^{+9.1}_{-7.8}$ per cent of the sample show extended radio structures indicative of AGN-driven outflows (i.e. jet or wind-driven; Fig. 3). This is compared to the $55^{+7.5}_{-7.7}$ per cent AGN-like extended radio structures for the more radio luminous QFeedS-1 quasars, which are also more likely to exhibit the most extended, $\gtrsim$10 kpc scale emission (Fig. 4).

(iii) Nine of the quasars display collimated morphologies indicative of AGNs (e.g. bipolar features, hot spots, S-shaped jets), although typically smaller in scale than classical FR I/II galaxies (Fig. 3; M. E. Jarvis et al. 2021; A. Njeri et al. 2025). Others (20/29) remain compact (Fig. 2) and may host sub-kpc jets, thus requiring higher resolution radio imaging to confirm (e.g. A. Njeri et al. 2025).

(iv) The majority (90 per cent) of the sample show very steep spectral indices across 5–7 GHz with $\alpha \lesssim -1$, potentially indicating a strong contribution from interactions between the AGN and

Downloaded from https://academic.oup.com/mnras/article/546/4/stag097/8427327 by University of Hertfordshire user on 18 February 2026

ISM. Only three QFeedS-2 sources show radio emission dominated by AGN-core like emission, based on flat spectral indices or high brightness temperatures (see Fig. 5).

(v) Combining spectral indices, brightness temperatures, and morphology criteria, 11/29 of the targets (i.e. $38^{+9.3}_{-8.5}$ per cent) are confirmed as radio AGNs. This is compared to 28/42 ($67^{+6.8}_{-7.6}$ per cent) following the same criteria, in the more radio-luminous QFeedS-1 sample (Section 5.1; Fig. 6). However, the total fraction of QFeedS-1 confirmed as radio AGNs is 86 per cent based on additional data from *e*-MERLIN and far-infrared measurements, which are not currently available for QFeedS-2 (Fig. 6; A. Njeri et al. 2025). Hence, 38 per cent is considered a lower limit of radio AGNs in QFeedS-2. Overall, $66^{+5.8}_{-5.9}$ per cent of the full QFeedS sample can be attributed to a radio-AGN origin.

(vi) For the sources that are not identified as a radio AGN ($\sim 62^{+8.5}_{-9.3}$ per cent) in QFeedS-2, it is not possible to rule out a strong contribution of star formation to the radio emission. However, across the sample as a whole, the radio emission is unlikely to be star-formation-dominated, due to the compact emission and very high inferred star formation rates at the radio luminosity range of the sample (Fig. 7).

(vii) Across the whole of QFeedS, the Type 2 sources display a slightly higher incidence of extended radio structures (52 per cent compared to 32 per cent). Furthermore, at the highest radio luminosities, the Type 1 sources are more likely to be core-dominated (with high brightness temperatures and flat spectral indices), compared to the Type 2 sources (Fig. 6). These observations are broadly consistent with an orientation based model of AGN types.

(viii) With $\sim$ 80 per cent of our QFeedS-2 sample falling in the FR0 region (Fig. 4), their radio properties would, at face value, be consistent with with the classical FR0 population (R. D. Baldi et al. 2015; R. D. Baldi 2023). However, by construction, our sample is selected to have very high [O III] luminosities ($L_{[\mathrm{O\,III}]} \geq 10^{42}\,\mathrm{erg\,s^{-1}}$), unambiguously pointing to radiatively efficient high-accretion quasars. This highlights that FR0-like radio morphologies do not necessarily imply radiatively inefficient accretion (Section 5.3).

The QFeedS demonstrates that quasars, even those traditionally labelled radio quiet, are not radio silent but span a continuous spectrum of radio activity and feedback modes; from powerful jets in luminous systems to weaker radio emission in lower luminosity systems, likely associated with weak radio jets or outflows from quasar winds. These results emphasize that robust identification of radio AGNs in the radio-quiet regime requires high-resolution multiband radio data, ideally combined with multi-wavelength constraints.

Our QFeedS-1 sample, which represents the higher radio luminosities ($L_{1.4\,\mathrm{GHz}} \sim 10^{23.45-26.30}\,\mathrm{W\,Hz^{-1}}$), has already revealed that compact AGN-driven jets and/or winds strongly couple to the ISM, driving significant multiphase outflows (e.g. M. E. Jarvis et al. 2021; A. Girdhar et al. 2022, 2024 ; S. Silpa et al. 2022). However, these objects align with the classical 'radio-intermediate' population where compact but powerful radio activity is becoming a clear signature of feedback activity (C. M. Harrison & C. Ramos Almeida 2024). Follow-up observations of QFeedS-2 will assess the driving mechanisms and impact on the ISM of lower radio power systems. Thus, the combined QFeedS quasars, covering four orders of magnitude in radio luminosity, represent a compelling laboratory for bridging radio-quiet and radio-loud AGN regimes, uncovering the diverse physical channels through which quasars generate radio emission, and how they can influence their galactic environments.

More broadly, current and future radio facilities (e.g. LOFAR-ILT, SKA, and ngVLA; P. E. Dewdney et al. 2009; E. J. Murphy et al. 2018; L. K. Morabito et al. 2025a) will be transformative in understanding radio emission and related feedback processes across the whole AGN population. High-frequency arrays will unveil low power milliarcsecond jets unidentified in current radio maps, while low-frequency high-sensitivity observations will capture aged diffuse plasma, which is key to understanding the full lifecycle of AGN outflows. Integrating such radio diagnostics with X-ray observations, sub-mm interferometry and integral-field spectroscopy, will allow us to directly observe how compact jets or quasar-driven winds impact the surrounding ISM and assess their role in feedback processes in large and representative AGN samples.

ACKNOWLEDGEMENTS

We thank the referee for their prompt and constructive report. AN, CMH, and VF acknowledge funding from an United Kingdom Research and Innovation grant (code: MR/V022830/1). PK acknowledges the support of the Department of Atomic Energy, Government of India, under the project 12-R&D-TFR-5.02-0700. DMA thanks the Science Technology Facilities Council (STFC) for support through the Durham consolidated grant (ST/T000244/1). SS acknowledges funding from ANID through Fondecyt Postdoctorado (project code 3250762), Millenium Nucleus NCN23_002 (TITANs), and Comité Mixto ESO-Chile. We acknowledge the use of the ilifu cloud computing facility – www.ilifu.ac.za, a partnership between the University of Cape Town, the University of the Western Cape, the University of Stellenbosch, Sol Plaatje University, the Cape Peninsula University of Technology, and the South African Radio Astronomy Observatory.

DATA AVAILABILITY

The data underlying this article were accessed from the NRAO Science Data Archive (https://data.nrao.edu/portal/) using the proposal id: 23A-214. The spectral index, *C*-band, and *L*-band maps produced in this work, including the figures for all 29 targets showing the radio contours overlaid on the optical images (in the style of Fig. 2), are all available at https://doi.org/10.25405/data.ncl.c.8110946. All public data related to the Quasar Feedback Survey can also be located via our website: https://blogs.ncl.ac.uk/quasarfeedbacksurvey/data/.

REFERENCES

Abazajian K. N. et al., 2009, ApJS, 182, 543
Ahumada R. et al., 2020, ApJS, 249, 3
An T., Baan W. A., 2012, ApJ, 760, 77
Audibert A. et al., 2023, A&A, 671, L12
Baldi R. D., 2023, A&AR, 31, 3
Baldi R. D., Capetti A., Giovannini G., 2015, A&A, 576, A38
Baldi R. D. et al., 2018, MNRAS, 476, 3478
Baldi R. D., Giovannini G., Capetti A., 2021, Galaxies, 9, 106
Becker R. H., White R. L., Helfand D. J., 1995, ApJ, 450, 559
Begelman M. C., Blandford R. D., Rees M. J., 1984, Rev. Mod. Phys., 56, 255
Behar E., Baldi R. D., Laor A., Horesh A., Stevens J., Tzioumis T., 2015, MNRAS, 451, 517

Downloaded from https://academic.oup.com/mnras/article/546/4/stag097/8427327 by University of Hertfordshire user on 18 February 2026

Bernhard E., Tadhunter C. N., Pierce J. C. S., Dicken D., Mullaney J. R., Morganti R., Ramos Almeida C., Daddi E., 2022, MNRAS, 512, 86
Bessiere P. S., Ramos Almeida C., Holden L. R., Tadhunter C. N., Canalizo G., 2024, A&A, 689, A271
CASA Team,, 2022, IMFIT – Image analysis task (image fitting). National Radio Astronomy Observatory (NRAO)/CASA Development Team, https://casa.nrao.edu/casadocs (accessed 01 December 2025)
Calistro Rivera G. et al., 2024, A&A, 691, A191
Chilufya J., Hardcastle M. J., Pierce J. C. S., Croston J. H., Mingo B., Zheng X., Baldi R. D., Röttgering H. J. A., 2024, MNRAS, 529, 1472
Circosta C. et al., 2018, A&A, 620, A82
Condon J. J., 1992, ARA&A, 30, 575
Condon J. J., Condon M. A., Gisler G., Puschell J. J., 1982, ApJ, 252, 102
Condon J. J., Huang Z.-P., Yin Q. F., Thuan T. X., 1991, ApJ, 378, 65
Condon J. J., Cotton W. D., Greisen E. W., Yin Q. F., Perley R. A., Taylor G. B., Broderick J. J., 1998, AJ, 115, 1693
Cresci G. et al., 2023, A&A, 672, A128
Davies R. et al., 2020, MNRAS, 498, 4150
de Vries W. H., Becker R. H., White R. L., Helfand D. J., 2004, AJ, 127, 2565
Del Moro A. et al., 2013, A&A, 549, A59
Delhaize J. et al., 2017, A&A, 602, A4
Delvecchio I. et al., 2017, A&A, 602, A3
Dewdney P. E., Hall P. J., Schilizzi R. T., Lazio T. J. L. W., 2009, Proc. IEEE, 97, 1482
Dey A. et al., 2019, AJ, 157, 168
Eberhard J.-M., Reines A. E., Gim H. B., Darling J., Greene J. E., 2025, ApJ, 978, 158
Fabian A. C., 2012, ARA&A, 50, 455
Fawcett V. A., Alexander D. M., Rosario D. J., Klindt L., Fotopoulou S., Lusso E., Morabito L. K., Calistro Rivera G., 2020, MNRAS, 494, 4802
Fawcett V. A. et al., 2025, MNRAS, 537, 2003
Fluetsch A. et al., 2021, MNRAS, 505, 5753
García-Burillo S. et al., 2021, A&A, 652, A98
Girdhar A. et al., 2022, MNRAS, 512, 1608
Girdhar A. et al., 2024, MNRAS, 527, 9322
Godfrey L. E. H., Shabala S. S., 2016, MNRAS, 456, 1172
Hardcastle M. J., Croston J. H., 2020, New Astron. Rev., 88, 101539
Hardcastle M. J. et al., 2025, MNRAS, 539, 1856
Harrison C. M., 2017, Nat. Astron., 1, 0165
Harrison C. M., Ramos Almeida C., 2024, Galaxies, 12, 17
Harrison C. M., Alexander D. M., Mullaney J. R., Swinbank A. M., 2014, MNRAS, 441, 3306
Harrison C. M., Thomson A. P., Alexander D. M., Bauer F. E., Edge A. C., Hogan M. T., Mullaney J. R., Swinbank A. M., 2015, ApJ, 800, 45
Harwood J. J. et al., 2022, A&A, 658, A8
Heckman T. M., Best P. N., 2014, ARA&A, 52, 589
Helou G., Soifer B. T., Rowan-Robinson M., 1985, ApJ, 298, L7
Ilha G. S. et al., 2025, A&A, 704, A293
Ivezić Ž. et al., 2002, AJ, 124, 2364
Jackson T. M., Rosario D. J., Alexander D. M., Scholtz J., McAlpine S., Bower R. G., 2020, MNRAS, 498, 2323
Jarvis M. E. et al., 2019, MNRAS, 485, 2710
Jarvis M. E. et al., 2020, MNRAS, 498, 1560
Jarvis M. E. et al., 2021, MNRAS, 503, 1780
Karouzos M., Woo J.-H., Bae H.-J., 2016, ApJ, 819, 148
Kellermann K. I., Sramek R., Schmidt M., Shaffer D. B., Green R., 1989, AJ, 98, 1195
Kellermann K. I., Condon J. J., Kimball A. E., Perley R. A., Ivezić Ž., 2016, ApJ, 831, 168
Kennicutt R. C., Evans N. J., 2012, ARA&A, 50, 531
Kewley L. J., Heisler C. A., Dopita M. A., Sutherland R., Norris R. P., Reynolds J., Lumsden S., 2000, ApJ, 530, 704
Kharb P., Silpa S., 2023, Galaxies, 11, 27
Kharb P., Vaddi S., Sebastian B., Subramanian S., Das M., Paragi Z., 2019, ApJ, 871, 249
Kharb P., Subramanian S., Das M., Vaddi S., Paragi Z., 2021, ApJ, 919, 108
Klindt L., Alexander D. M., Rosario D. J., Lusso E., Fotopoulou S., 2019, MNRAS, 488, 3109
Kunert-Bajraszewska M., Gawroński M. P., Labiano A., Siemiginowska A., 2010, MNRAS, 408, 2261
Laing R. A., Peacock J. A., 1980, MNRAS, 190, 903
Lansbury G. B., Jarvis M. E., Harrison C. M., Alexander D. M., Del Moro A., Edge A. C., Mullaney J. R., Thomson A. P., 2018, ApJ, 856, L1
Laor A., Behar E., 2008, MNRAS, 390, 847
Liao M., Wang J., Ren W., Zhou M., 2024, MNRAS, 528, 3696
Magliocchetti M., Popesso P., Brusa M., Salvato M., 2018, MNRAS, 473, 2493
Marvil J., Owen F., Eilek J., 2015, AJ, 149, 32
McCaffrey T. V., Kimball A. E., Momjian E., Richards G. T., 2022, AJ, 164, 122
McMullin J. P., Waters B., Schiebel D., Young W., Golap K., 2007, in Shaw R. A., Hill F., Bell D. J., eds, ASP Conf. Ser. Vol. 376, Astronomical Data Analysis Software and Systems XVI, Astron. Soc. Pac., San Francisco, San Francisco, p. 127
Meenakshi M. et al., 2022, MNRAS, 516, 766
Meenakshi M., Mukherjee D., Bodo G., Rossi P., Harrison C. M., 2024, MNRAS, 533, 2213
Middelberg E., Agudo I., Roy A. L., Krichbaum T. P., 2007, MNRAS, 377, 731
Mingo B. et al., 2022, MNRAS, 511, 3250
Molyneux S. J. et al., 2024, MNRAS, 527, 4420
Mooley K. P. et al., 2016, ApJ, 818, 105
Morabito L. K. et al., 2022, MNRAS, 515, 5758
Morabito L. K. et al., 2025a, Ap&SS, 370, 19
Morabito L. K. et al., 2025b, MNRAS, 536, L32
Morganti R., Tadhunter C. N., Oosterloo T. A., 2005, A&A, 444, L9
Morganti R., Murthy S., Guillard P., Oosterloo T., Garcia-Burillo S., 2023, Galaxies, 11, 24
Mukherjee D., 2025, Galaxies, 13, 102
Mukherjee D., Bicknell G. V., Wagner A. Y., Sutherland R. S., Silk J., 2018, MNRAS, 479, 5544
Mullaney J. R., Alexander D. M., Fine S., Goulding A. D., Harrison C. M., Hickox R. C., 2013, MNRAS, 433, 622
Murphy E. J. et al., 2011, ApJ, 737, 67
Murphy E. J. et al., 2018, in Murphy E. ed., ASP Conf. Ser. Vol. 517, Science with a Next Generation Very Large Array. Astron. Soc. Pac., San Francisco, p. 3
Nesvadba N. P. H., De Breuck C., Lehnert M. D., Best P. N., Collet C., 2017, A&A, 599, A123
Nims J., Quataert E., Faucher-Giguère C.-A., 2015, MNRAS, 447, 3612
Njeri A. et al., 2023, MNRAS, 519, 1732
Njeri A. et al., 2025, MNRAS, 537, 705
O'Dea C. P., 1998, PASP, 110, 493
O'Dea C. P., Saikia D. J., 2021, A&AR, 29, 3
Ofek E. O., Frail D. A., 2011, ApJ, 737, 45
Padovani P., 2016, A&AR, 24, 13
Padovani P., 2017, Nat. Astron., 1, 0194
Panessa F., Baldi R. D., Laor A., Padovani P., Behar E., McHardy I., 2019, Nat. Astron., 3, 387
Perley R. A., Butler B. J., 2013, ApJS, 204, 19
Pierce J. C. S., Tadhunter C. N., Morganti R., 2020, MNRAS, 494, 2053
Radcliffe J. F. et al., 2018, A&A, 619, A48
Radcliffe J. F., Beswick R. J., Thomson A. P., Garrett M. A., Barthel P. D., Muxlow T. W. B., 2019, MNRAS, 490, 4024
Ramos Almeida C. et al., 2022, A&A, 658, A155
Rao V. V. et al., 2023, MNRAS, 524, 1615
Riffel R. A., Storchi-Bergmann T., Riffel R., Dahmer-Hahn L. G., Diniz M. R., Schönell A. J., Dametto N. Z., 2017, MNRAS, 470, 992
Rosario D. J., Fawcett V. A., Klindt L., Alexander D. M., Morabito L. K., Fotopoulou S., Lusso E., Calistro Rivera G., 2020, MNRAS, 494, 3061
Rose M., Tadhunter C., Ramos Almeida C., Rodríguez Zaurín J., Santoro F., Spence R., 2018, MNRAS, 474, 128
Roy N., Heckman T., Henry A., 2025, preprint (arXiv:2508.06707)
Sabater J. et al., 2019, A&A, 622, A17

Downloaded from https://academic.oup.com/mnras/article/546/4/stag097/8427327 by University of Hertfordshire user on 18 February 2026

Santoro F., Tadhunter C., Baron D., Morganti R., Holt J., 2020, A&A, 644, A54
Shimizu T. T., Mushotzky R. F., Meléndez M., Koss M. J., Barger A. J., Cowie L. L., 2017, MNRAS, 466, 3161
Silpa S., Kharb P., Ho L. C., Ishwara-Chandra C. H., Jarvis M. E., Harrison C., 2020, MNRAS, 499, 5826
Silpa S., Kharb P., Harrison C. M., Girdhar A., Mukherjee D., Mainieri V., Jarvis M. E., 2022, MNRAS, 513, 4208
Silpa S., Kharb P., Ho L. C., Harrison C. M., 2023, ApJ, 958, 47
Slob M. M., Callingham J. R., Röttgering H. J. A., Williams W. L., Duncan K. J., de Gasperin F., Hardcastle M. J., Miley G. K., 2022, A&A, 668, A186
Smolčić V. et al., 2017, A&A, 602, A6
Speranza G. et al., 2021, A&A, 653, A150
Tadhunter C., 2016, Astron. Nachr., 337, 159
Tanner R., Weaver K. A., 2022, AJ, 163, 134
Ulivi L. et al., 2024, A&A, 685, A122
Ulvestad J. S., Antonucci R. R. J., Barvainis R., 2005, ApJ, 621, 123
Venturi G. et al., 2021, A&A, 648, A17
Villar Martín M., Emonts B. H. C., Cabrera Lavers A., Bellocchi E., Alonso Herrero A., Humphrey A., Dall'Agnol de Oliveira B., Storchi-Bergmann T., 2021, A&A, 650, A84
Wang Y. et al., 2024, A&A, 685, A79
White S. V., Jarvis M. J., Häußler B., Maddox N., 2015, MNRAS, 448, 2665
White S. V., Jarvis M. J., Kalfountzou E., Hardcastle M. J., Verma A., Cao Orjales J. M., Stevens J., 2017, MNRAS, 468, 217
Woo J.-H., Bae H.-J., Son D., Karouzos M., 2016, ApJ, 817, 108
Xu C., Livio M., Baum S., 1999, AJ, 118, 1169
Yun M. S., Reddy N. A., Condon J. J., 2001, ApJ, 554, 803
Zakamska N. L., Greene J. E., 2014, MNRAS, 442, 784
Zakamska N. L., Strauss M. A., Heckman T. M., Ivezić Ž., Krolik J. H., 2004, AJ, 128, 1002
Zakamska N. L. et al., 2016, MNRAS, 455, 4191

This paper has been typeset from a TEX/LATEX file prepared by the author.

Downloaded from https://academic.oup.com/mnras/article/546/4/stag097/8427327 by University of Hertfordshire user on 18 February 2026

© The Author(s) 2026.
Published by Oxford University Press on behalf of Royal Astronomical Society. This is an Open Access article distributed under the terms of the Creative Commons Attribution License (https://creativecommons.org/licenses/by/4.0/), which permits unrestricted reuse, distribution, and reproduction in any medium, provided the original work is properly cited.